Title: Tracking H3K27me3 and H4K20me1 dynamics during XCI reveals similarities in recruitment mechanism

#Sjoerd J. D. Tjalsma[1], #Mayako Hori[2], #Yuko Sato[2, 3], Aurelie Bousard[1], Akito Ohi[2], Ana Cláudia Raposo[4], Julia Roensch[1], Agnes Le Saux[1], Jumpei Nogami[5], Kazumitsu Maehara[5], Tomoya Kujirai[6], Yasuyuki Ohkawa[5], Hitoshi Kurumizaka[6], Simão Teixeira da Rocha[4], *Jan J. Żylicz[1, 7, 8], *Hiroshi Kimura[2, 3], *Edith Heard[9]

# these authors contributed equally
* Corresponding author: jan.zylicz@sund.ku.dk
* Corresponding author: hkimura@bio.titech.ac.jp
* Corresponding author: edith.heard@embl.org

1 Mammalian Developmental Epigenetics Group, Institut Curie, CNRS UMR3215, INSERM U934, PSL University, Paris, France
2 Graduate School of Bioscience and Biotechnology, Tokyo Institute of Technology, Yokohama, Japan
3 Cell Biology Center, Institute of Innovative Research, Tokyo Institute of Technology, Yokohama, Japan.
4 Instituto de Medicina Molecular, João Lobo Antunes, Faculdade de Medicina, Universidade de Lisboa, Lisboa, Portugal.
5 Division of Transcriptomics, Medical Institute of Bioregulation, Kyushu University, Fukuoka, Japan
6 Institute for Quantitative Biosciences, The University of Tokyo, Tokyo, Japan
7 Department of Physiology, Development and Neuroscience, University of Cambridge, Cambridge, UK
8 Current address: The Novo Nordisk Foundation Center for Stem Cell Biology, Copenhagen, Denmark.
9 Directors' Research, EMBL Heidelberg, 69117 Heidelberg, Germany

Abstract :

During X chromosome inactivation (XCI), in female mammals, gene silencing is initiated by the Xist long-noncoding RNA. Xist accumulation at the X leads to enrichment of specific chromatin marks, including PRC2-dependent H3K27me3 and SETD8-dependent H4K20me1. However, the dynamics of this process in relation to Xist RNA accumulation remains unknown as is the molecular mechanism allowing for H4K20me1 enrichment. To follow XCI dynamics in living cells, we developed a genetically-encoded, H3K27me3-specific intracellular antibody, or H3K27me3-mintbody. By combining it with live-imaging of H4K20me1, the X chromosome and Xist RNA we uncover similarities in the initial accumulation dynamics of H3K27me3 and H4K20me1. Further ChIP-seq analysis confirmed concurrent accumulation of both marks during XCI albeit with distinct genomic distributions. Using a Xist B and C repeat mutant, which can silence the X but does not allow for H3K27me3 enrichment, we also found a lack of H4K20me1 deposition. Thus, these two marks are brought onto the X by the same region of Xist and H4K20me1 in particular may well have a role in the chromatin compaction that characterises facultative heterochromatin.

Introduction :

Dynamic changes to the chromatin landscape allow for timely execution of developmental and differentiation programmes. Indeed, chromatin modifiers often reinforce signalling cues to initiate and/or maintain an exact transcriptional outcome (Jambhekar, Dhall et al., 2019,

Stasevich, Hayashi-Takanaka et al., 2014, Zylicz, Dietmann et al., 2015). One powerful model, where such regulation takes place is X chromosome inactivation (XCI) in female mammals. Although much is known about the involvement of certain chromatin marks in initiating XCI (reviewed in (Zylicz & Heard, 2020), it was thus far impossible to track chromatin rearrangements and the inactive X chromosome (Xi) in living cells. What is more, the role and dynamics of some histone modifications during XCI remains enigmatic.

In eutherian female mammals XCI is initiated at around the time of implantation, when each cell randomly inactivates one of the two X chromosomes (Lyon, 1962). This process can be modelled in vitro by differentiating female mouse embryonic stem cells (ESC) (Rastan & Robertson, 1985). Both in vivo and in vitro, XCI depends on the coating of the Xi by a long non-coding RNA called *Xist* (X-inactive-specific transcript) (Penny, Kay et al., 1996). *Xist* RNA accumulation along the Xi induces not only the silencing of over a 1000 genes but also a cascade of chromatin alterations (reviewed in: (Zylicz & Heard, 2020)). *Xist* is a modular non-coding RNA with specific regions playing distinct roles. Its 5' A-repeat region is vital for the induction of gene silencing (Wutz, Rasmussen et al., 2002). It does so by recruiting SPEN, a key RNA-binding protein, which integrates many repressive complexes including NCOR/SMRT and HDAC3 (Dossin, Pinheiro et al., 2020, McHugh, Chen et al., 2015, Zylicz, Bousard et al., 2019). On the other hand, the B and to a lesser extent C-repeat regions are vital for the recruitment of Polycomb-group repressive complexes (PRC) (Bousard, Raposo et al., 2019, Colognori, Sunwoo et al., 2019, Nesterova, Wei et al., 2019). Indeed, upon *Xist* RNA coating Xi becomes rapidly enriched with the PRC1-dependent H2AK119Ub and only subsequently with PRC2-dependent H3K27me3 (de Napoles, Mermoud et al., 2004, Plath, Fang et al., 2003, Silva, Mak et al., 2003, Zylicz et al., 2019). Recent data indicate that the B and C-repeat region of *Xist* RNA directly recruits hnRNPK, which in turn binds non-canonical PRC1 allowing for rapid H2AK119Ub deposition (Almeida, Pintacuda et al., 2017, Bousard et al., 2019, Colognori et al., 2019, Pintacuda, Wei et al., 2017). H2AK119Ub could potentially be recognised by PRC2 co-factors allowing for de novo deposition of H3K27me3 (Blackledge, Farcas et al., 2014). Importantly, Polycomb accumulation is dispensable for the initiation of gene silencing, as *Xist* mutants lacking the B and C repeat region can still induce XCI albeit with slightly lower efficiency (Bousard et al., 2019, Nesterova et al., 2019). Instead, PRC2 enables stable maintenance of the repressed state, particularly in the context of extra-embryonic lineages (Kalantry, Mills et al., 2006). The dynamics of accumulation of PcG marks have been studied using ChIP-seq, although it remains unclear how precisely this correlates with *Xist* RNA coating of the Xi. Indeed, the time that lapses between *Xist* RNA upregulation and H3K27me3 deposition is not known. Nor how this relates to other repressive histone marks.

Another modification that rapidly accumulates on the Xi is H4K20me1 (Kohlmaier, Savarese et al., 2004), although its role in XCI is not well understood. H4K20me1 is deposited by SETD8 (also called Pr-Set7) (Nishioka, Rice et al., 2002) and is thought to regulate a variety of processes relating to transcription, chromosome condensation, DNA replication and the DNA damage response (reviewed in (van Nuland & Gozani, 2016)). Consistent with the involvement of H4K20me1 in cell division, it transiently accumulates during G2 and mitosis whereas H4K20me2 and -me3 do not show similar fluctuations during the cell cycle (Wu, Wang et al., 2010). This dynamics is achieved by stable expression of SETD8 during G2/M when its phosphorylation prevents the interaction with the Anaphase Promoting Complex (APC). During late mitosis CDC14 dephosphorylates SETD8 thus stimulating its degradation by APC. On the other hand PHF8, H4K20me1 demethylase, is degraded by APC during early G2 (Lim, Dimova et al., 2013) together allowing for transient deposition of H4K20me1 and successful progression through mitosis. Furthermore, H4K20me1 accumulates at centromeres where it promotes kinetochore assembly and thus correct chromosome segregation (Hori, Shang et al., 2014). The regulation of H4K20me1 levels could also be achieved by demethylating H4K20me2/3 by specific enzymes. DPNY-21 mediates such a reaction in Caenorhabditis elegans, and its two mouse orthologs (RSBN1/RSBN1L) retain

specific demethylase activity in vitro (Brejc, Bian et al., 2017). However, the biological function of these enzymes remains unknown. The study of H4K20me1 during XCI has been hampered by the fact that SETD8 is absolutely required for the progression through mitosis and embryos lacking it die before the onset of XCI (Oda, Okamoto et al., 2009, Shikata, Yamamoto et al., 2020). While the genomic distribution of H4K20me1 at a stably inactivated X was previously described (Calabrese, Sun et al., 2012), the dynamics of H4K20me1 accumulation during XCI initiation in relation to *Xist* RNA and H3K27me3 deposition remains unclear. Furthermore the precise distribution of first H4K20me1 enrichment along the X and the molecular mechanisms underlying its dynamic accumulation on the Xi have not previously been investigated.

To address these questions it is important to follow the spatio-temporal dynamics of histone modifications as they accumulate on the X chromosome in living cells. To this end we have previously developed genetically encoded, modification-specific intracellular antibodies, or mintbodies, by fusing a single-chain variable fragment (scFv) of the specific antibody with a fluorescent protein (Sato, Kujirai et al., 2016, Sato, Mukai et al., 2013). The expression of mintbodies enables tracking of changes in endogenous histone modification levels without affecting cell cycle progression and developmental processes in such model organisms as fission yeast, nematode, drosophila, and zebrafish (Arai, Sugawara et al., 2017, Sato et al., 2013). Here, to follow XCI dynamics in living cells, we developed a mintbody specific for the PRC2-dependent H3K27me3. In addition, we implemented sgRNA-dCas9 system to visualise both X chromosomes in living cells (Anton, Bultmann et al., 2014, Chen, Gilbert et al., 2013). We used these novel tools in combination with an H4K20me1-specific mintbody (Sato et al., 2016) and a method to visualise endogenous *Xist* RNA in live cells (Dossin et al., 2020, Masui, Heard et al., 2018). This allowed us to show that there are striking similarities in the accumulation dynamics of both H3K27me3 and H4K20me1 marks on the Xi. Further ChIP-seq analysis confirmed concurrent accumulation of H4K20me1 and H3K27me3 during XCI albeit with rather distinct genomic distributions and correlations with gene silencing dynamics. By using cells expressing mutant *Xist* RNA we demonstrate that H4K20me1 accumulation, just like that of PcG-dependent H3K27me3, relies on the *Xist* RNA B and C repeats. This also reveals that both marks are dispensable for the initiation of gene silencing. Taken together, our analysis uncovers that the H4K20me1 and H3K27me3 histone marks accumulate at the Xi with comparable dynamics but with rather different distributions. This points to common recruitment but distinct deposition mechanisms as the facultative heterochromatin of the inactive X is formed.

Results :

H3K27me3 mintbody (2E12LI) specifically tracks H3K27me3 in living cells

Methods for tracking polycomb-dependent histone marks in living cells have been lacking up until now. Such tools would be hugely beneficial for the study of dynamic epigenetic processes such as XCI. To address this we decided to generate an H3K27me3-specific mintbody. Upon screening of mouse hybridomas we selected a 2E12 clone, which expresses an H3K27me3-specific antibody. We determined the cDNA sequence of the IgG heavy and light chains in 2E12 by deep sequencing (Kuniyoshi, Maehara et al., 2016) and cloned the variable fragments by PCR to construct a mintbody expression vector (**Fig. 1A** and **EV1A**). To validate that the mintbody properly localizes to H3K27me3-enriched chromatin in living cells, we used mouse teratocarcinoma cell line MC12 (Abe, Takagi et al., 1988). MC12 is a mixture of diploid and tetraploid female cells harboring one or two Xi, on which the mintbody is expected to be concentrated. When expressed in MC12, the superfolder (sf) GFP version of 2E12 mintbody (2E12-sfGFP) localized mostly in cytoplasm and tended to form aggregates (**Fig. EV1B**, left), suggesting that 2E12-sfGFP was not able to function in cells, probably due to a typical problem in folding and/or structural stability associated with the intracellular expression of scFv (Cattaneo & Biocca, 1999, Ewert, Honegger et al., 2004). To prevent aggregate formation, we performed PCR-based random mutagenesis and transient

transfection into MC12 cells. One mutant that localized preferentially in the nucleus with focal enrichment (presumably Xi) had Met 86 to Leu substitution in the heavy chain (M86L) (Fig. **EV1B**, middle). Changes in localization suggested that M86L mutation improved the mintbody function to bind to H3K27me3. To gain insight into the contribution of M86L mutation in scFv structure, we looked into the atomic models built based on the X-ray structure of the most similar scFv (**Fig. EV1C**, left). The modeling indicated that Met 86 is located within a hydrophobic core of the heavy chain and its substitution to Leu appears to fill the space in the core better than the original Met to strengthen hydrophobic interactions. We have previously observed that the hydrophobicity of an amino acid in a hydrophobic core is important for the functionality of a H4K20me1-mintbody (Sato et al., 2016). However, the 2E12M86L-sfGFP was still not exclusively located in the nucleus and we were unable to obtain cells stably expressing it. Thus, we decided to further strengthen scFv folding with an additional mutation at Met 158 in the light chain's hydrophobic core (**Fig. EV1C**, right). We constructed three mutants in which Met 158 was substituted to Ile, Leu, and Val in 2E12M86L. Among the three mutations, M185I mutant was the most enriched in the nucleus with evident foci (**Fig. EV1B**, right). To confirm that nuclear foci of 2E12M86L, M185I (2E12LI)-sfGFP represent H3K27me3-enriched Xi, we employed immunofluorescence (IF) on transiently expressing cells using previously characterized specific antibodies directed against H3K27me3 and H3K9me3 (CMA327 and CMA318, respectively; (Chandra, Kirschner et al., 2012)). The nuclear foci were colocalized with a H3K27me3-specific antibody, but not with H3K9me3-specific antibody that is concentrated in Hoechst-dense pericentromeric heterochromatin (**Fig. 1B**). This data is consistent with the mintbody foci representing Xi in living cells. The utility of 2E12LI mintbody was further demonstrated by time-lapse imaging of stably expressing MC12 cells, which allowed for the tracking of Xi during interphase and mitosis (**Fig. 1C** and **Movie EV1**).

To further validate the specificity of 2E12LI to H3K27me3, we performed both biochemical and cell-based assays. We first evaluated the binding specificity of bacterially expressed and purified 2E12LI-sfGFP in vitro using a modified histone peptide array (**Fig. EV2A**). H3K27me3-containing peptides were highlighted over other peptides, regardless of the neighboring R26 modifications (**Fig. EV2B**). The 2E12LI-sfGFP binding was however occluded by S28 phosphorylation (S28ph), as commonly observed for methyl-specific antibodies (Hayashi-Takanaka, Yamagata et al., 2011, Kimura, 2013, Kimura, Hayashi-Takanaka et al., 2008). Next, we assessed if the purified 2E12LI-sfGFP can selectively bind to H3K27me3 in cells by manipulating the level of specific methylation. HeLa cells were transfected with HaloTag-tagged lysine demethylases KDM6B and KDM4D and fixed for staining with the specific antibodies or 2E12LI-sfGFP. Consistently with the substrate specificity of these KDMs, IF indicated that HeLa cells overexpressing Halo-KDM6B and Halo-KDM4D exhibited drastic decrease of H3K27me3 and H3K9me3, respectively (**Fig. EV2C, D**). The result of staining with purified 2E12LI-scFv was similar to H3K27me3-specific antibody, showing decreased levels of H3K27me3 by Halo-KDM6B overexpression and no changes in H3K27me3 by Halo-KDM4D (**Fig. EV2E, F**). Taken together with the immunofluorescence pattern and biochemical analysis, we concluded that 2E12LI-sfGFP selectively binds to H3K27me3 over the other modifications including H3K9me3. For convenience, we now call 2E12LI fused with a fluorescent protein as H3K27me3-mintbody.

Simultaneous tracking of X chromosome loci, H3K27me3 and H4K20me1 during XCI

In order to visualize the dynamics of histone modifications during XCI, we decided to develop a method to identify the X chromosome in live cells. We used an sgRNA-dCas9 (single guide RNA-nuclease dead Cas9) system to label X-linked loci in living cells (Anton et al., 2014, Ma, Naseri et al., 2015). We screened repetitive sequences located specifically on the mouse X chromosome and chose 32 microsatellite sequences as target candidates. The expression vectors for sgRNAs that bind to the sequences were constructed and co-transfected with an

expression vector for EGFP-tagged dCas9 into MC12 cells. Among them, 4 sgRNAs (mX2, mX8, mX18, and mX26) enabled visualizing X-linked loci in living cells (**Fig. EV3**). We selected mX8 (near *Xist* locus) and mX26 (*Dxz4* locus) to label X chromosomes and used 3×sfGFP-tagged dCas9 (3×sfGFP-dCas9), to amplify the signal for further analyses using ESCs.

To track H3K27me3 during X-inactivation, we established female mouse ESCs (PGK12.1) expressing two sgRNA (mX8 and mX26), 3×sfGFP-dCas9, and H3K27me3-mintbody (mCherry version) (**Fig. 2A, B**). In undifferentiated ESCs, X chromosome loci were identified as 2 pairs of 3×sfGFP-dCas9 spots and H3K27me3-mintbody was not enriched in either allele (**Fig. 2C**, upper panels). In contrast, three days after withdrawal of leukemia inhibitory factor (LIF), H3K27me3-mintbody accumulated around one pair of 3×sfGFP-dCas9 spots (**Fig. 2C**, lower panels). This result demonstrated that H3K27me3-mintbody together with the sgRNA-dCas9 system allows for tracking the dynamics of histone modification in living and differentiating cells. Since H4K20me1 also becomes enriched on Xi (Kohlmaier et al., 2004), we sought to reveal the relative accumulation kinetics of the H3K27me3 and H4K20me1 histone modifications during XCI. We established mESCs expressing the two sgRNAs, 3×sfGFP-dCas9, H3K27me3-mintbody (mCherry version), and H4K20me1-mintbody (HaloTag version, visualized with JF646, (Sato et al., 2016)) and induced differentiation (3d LIF withdrawal).Time-lapse imaging revealed that whenever H3K27me3 accumulation was visible at the Xi, some level of H4K20me1 enrichment was also discernible (**Fig. 2D**), suggesting that both repressive marks accumulate concurrently during XCI. This initial analysis in differentiating female ESCs confirmed the successful use of both H3K27me3- and H4K20me1-mintbodies to follow enrichment of these two marks on the X chromosome. However, given the asynchronous nature of random XCI in differentiating ESCs and the rather weak signal from the tagged X-linked loci, it was challenging to distinguish the Xi from the active X (Xa) prior to a significant accumulation of both repressive chromatin marks on the Xi. To ameliorate our analysis, we therefore decided to follow *Xist* RNA itself in living cells alongside H3K27me3 or H4K20me1.

H3K27me3 accumulates concurrently with H4K20me1 at the Xi

In order to track the relative dynamics of H3K27me3, H4K20me1 and *Xist* RNA during XCI we combined the use of mintbodies with the inducible *Xist*-Bgl system (Dossin et al., 2020, Masui et al., 2018) (**Fig. 3A**). The latter model is based on the hybrid (*Mus musculus castaneus* x C57BL/6) TX1072 female ESCs line allowing for doxycycline (DOX) induction of the endogenous *Xist* gene from C57BL/6 (*B6*) allele (Schulz, Meisig et al., 2014). By adding DOX we can rapidly induce *Xist* expression and thus reduce the level of heterogeneity observed during XCI in differentiating ESCs. In addition, 18 Bgl RNA stem loops (BglSL) were knocked into the 7th exon of DOX-inducible *Xist* (**Fig. EV4A**) (Dossin et al., 2020). To track *Xist* RNA accumulation BglSL are visualised by a BglG protein fused to either EGFP or mCherry and expressed from the *Rosa26* or *TIGRE* locus (**Fig. EV4B-C**). The cell lines enabling *Xist* RNA visualisation are named TX-*Xist*-EGFP and TX-*Xist*-mCherry. These cell lines were used to generate stably expressing *PiggyBac* transgenes for the H3K27me3- or H4K20me1-mintbodies (**Fig. EV4B-C**). Two ESC lines, TX-*Xist*-EGFP; H4K20me1-mCherry and TX-*Xist*-mCherry; H3K27me3-sfGFP were used for subsequent analyses. Importantly, the use of *Xist*-BglSL or the mintbodies did not affect the efficiency of gene silencing during XCI (**Fig. EV4D**).

In order to visualise the earliest events following *Xist* RNA accumulation we started live-imaging of ESCs 5 minutes after DOX induction (**Fig. 3B, Movie EV2-3**). Imaging was performed for at least 6 hrs in 15 min intervals allowing for single-cell tracking and detailed quantitative analysis. *Xist* RNA domains were segmented using the *Xist*-EGFP/mCherry

signal. The mintbody enrichment within such domains was measured and followed in individual cells throughout the length of the experiment (**Fig. 3C**). Of note, unlike H3K27me3-mintbody, H4K20me1-mintbody shows increased nuclear signal during G2/M phase of the cell cycle, thus tracking the oscillations in H4K20me1 levels (Sato et al., 2016).We thus excluded mitotic cells from the analysis due to very high overall levels of H4K20me1. Next, we followed the enrichment of H3K27m3/H4K20me1 signal in at least 30 nuclei synchronized to the time-point when *Xist* RNA enrichment was first observed. A significant enrichment of both histone marks was observed within the *Xist* RNA domain about 45 min after *Xist*-RNA appearance (adj. p-value <0.05; **Fig. 3B-C**). Initial accumulation of H3K27me3 and H4K20me1 followed very similar dynamics. However after 2.5h the two marks significantly diverged (**Fig. 3C**). Indeed, H3K27me3 continued to rapidly accumulate, while the increase in H4K20me1 enrichment significantly slowed down (**Fig. 3C**). Thus we have successfully performed simultaneous tracking of *Xist* RNA and repressive histone marks. In summary, the enrichment of both H3K27me3 and H4K20me1 is delayed compared to *Xist* RNA accumulation by about 45 min. H3K27me3 shows a continued accumulation over time whilst that of H4K20me1 eventually slows down. This suggests that the two marks may share a similar recruitment mechanism to the Xi, even though their dynamics are not identical.

Allele-specific native ChIP-seq reveals similarities between H3K27me3 and H4K20me1 accumulation dynamics

Given the above results indicating that although H3K27me3 and H4K20me1 are both initially enriched soon after *Xist* RNA accumulation, their patterns diverge after a few hours, we decided to investigate the molecular distributions of both these marks along the Xi. To this end we performed allele-specific native ChIP-seq (nChIP-seq) for H4K20me1 in the hybrid female cell line TX1072 (Schulz et al., 2014). Thanks to an inducible *Xist* gene on the B6 chromosome, DOX addition leads to rapid gene silencing and chromatin mark alterations that can be measured allelically thanks to the high rate of polymorphism between the B6 and Cast X chromosomes (Zylicz et al., 2019). Following DOX treatment we tracked H4K20me1 accumulation on the *Xist* RNA coated B6 allele across five time points at up to 4-hr resolution on biological duplicates (**Fig. 4A**). We compared all our results with a matched published dataset of H3K27me3 (Zylicz et al., 2019). Importantly, we validated the specificity of H4K20me1 antibody using a peptide array (**Fig. EV5A**) and controlled for *Xist* RNA induction efficiency. Upon sequencing, reads were split according to content of allele-specific single nucleotide polymorphisms (SNPs: *B6* mapping to Xi; *Cast* mapping to Xa). Such allelic information was analysed, revealing progressive enrichment of B6-specific reads (originating from Xi) upon *Xist* induction for H4K20me1 as is the case for H3K27me3 (**Fig. EV5B**). We analysed relative *B6*-read enrichment within 10-kb windows across the whole X-chromosome normalised to t = 0hr (**Fig. 4B**). This revealed significant H4K20me1 accumulation after 8 hr of DOX induction, a time point when H3K27me3 also starts to accrue. However, the levels of enrichment observed for H4K20me1 are lower than for H3K27me3 and seem to reach their plateau earlier. To better visualise the timing of accumulation we normalised both marks to their effective dynamic range i.e. to average accumulation after 24 hr of DOX induction (**Fig. 4C**). This confirmed that after 8 hrs of DOX treatment there is concurrent initiation of H4K20me1 and H3K27me3 accumulation. To quantify this further we plotted the B6-read enrichment relative to t=0 hr of each 10-kb window as a function of time and fitted a sigmoidal curve (see Materials and Methods). To extract the information about relative timing of histone mark accumulation we obtained the time when each curve reaches its maximum slope (effective dose 50%, ED50). ED50 analysis revealed that H4K20me1 reaches its most efficient accumulation prior to H3K27me3 (**Fig. 4D**). This is in line with H4K20me1 achieving its plateau significantly before H3K27me3. Thus our analysis confirmed live-imaging observations that H4K20me1 accumulates concurrently with H3K27me3 but quickly reaches maximum enrichment (**Fig. 3C**).

We next examined the degree to which the distributions of the two marks overlapped across the Xi. We found that H4K20me1 becomes preferentially enriched at loci in proximity to the *Xist* gene (green bar) as well as at regions that *Xist* RNA first interacts with (so called “entry sites”, black bars (Pinter, Sadreyev et al., 2012))(**Fig. 4E**). The initial enrichment of H4K20me1 on the *Xist*-coated X follows the same pattern previously detected for not only H3K27me3 but also for PRC1-dependent H2AK119Ub (**Fig. 4E**)(Zylicz et al., 2019). To confirm this observation we investigated chromosome-wide correlation between H3K27me3 and H4K20me1 accumulation within different genomic windows (**Fig. 4F**). Consistently with our initial observation, we found striking correlation in the accumulation of both marks across intergenic windows as well as bodies of silent genes. In contrast, the bodies of genes that were active prior to DOX treatment (i.e. initially active genes) showed a much lower Pearson’s correlation with $\rho=0.2$ implying that both marks differ in their correlation with transcription. With the exception of initially active genes, nChIP-seq of H4K20me1 revealed that its accumulation follows a strikingly similar pattern and dynamics compared to H3K27me3. This indicates that both marks could initially accumulate at the Xi thanks to a common mechanism but further accumulation and spreading would use distinct mechanisms.

H4K20me1 accumulates intergenically and is dispensable for XCI initiation

The above nChIP-seq analysis revealed similarities and differences between H4K20me1 and H3K27me3 accumulation on the X during XCI. While investigating genes that are initially active and then become silenced following *Xist* induction, we observed that H4K20me1 is strongly biallelically enriched (pre-marked) at transcribed gene bodies, prior to silencing (**Fig. 5A**). This contrasts strikingly with the distribution of H3K27me3, which never pre-marks initially active genes (Zylicz et al., 2019) . We confirmed that this H4K20me1 enrichment at transcribed genes is a general feature both on the X chromosome (**Fig. 5B**) and autosomes (**Fig. EV5C**). This is in line with previous reports indicating that H4K20me1 correlates with transcriptional elongation and is enriched at active gene bodies (Beck, Oda et al., 2012, Kapoor-Vazirani & Vertino, 2014, Veloso, Kirkconnell et al., 2014). In this sense H4K20me1 seems to behave like an “active” chromatin mark. Upon *Xist* induction (+ DOX) we found a significant accumulation of H4K20me1 on the Xi at initially active promoters and intergenic regions (**Fig. 5A-B**). This resembles the pattern observed for H3K27me3, with the intriguing caveat that H4K20me1 does not seem to further accumulate at bodies of initially active genes, rather, H4K20me1 levels remain constant. Thus H4K20me1 and H3K27me3 accumulation patterns are strikingly similar within intergenic regions but differ in the bodies of initially active genes (**Fig. 4F**). Next, to evaluate the relationship between H4K20me1 accumulation and the process of gene silencing, we separately analysed genes inactivated early and late upon DOX treatment (**Fig. 5C**). This revealed that while H4K20me1 *de novo* accumulation following *Xist* induction is restricted to intergenic and promoter regions, it occurs more efficiently in the proximity of rapidly silenced genes e.g. of *Rnf12* (**Fig. 5A**). All in all, these findings suggest that prior to XCI, H4K20me1 correlates with active transcription (in gene bodies), but following *Xist* induction H4K20me1 becomes enriched de novo at regions surrounding genes that are rapidly silenced. The strong pre-marking of initially active genes indicates that H4K20me1 can behave as an “active” chromatin modification.

To further explore the potential relationship of H4K20me1 enrichment and H3K27me3 deposition during XCI we decided to investigate chromatin states in *Xist* mutant cell lines. Current models suggest that H3K27me3 is deposited thanks to a complex machinery, involving initial PRC1 recruitment by the B and C repeats of *Xist* and subsequent PRC2 recruitment thanks to H2AK119Ub enrichment (Almeida et al., 2017, Bousard et al., 2019, Colognori et al., 2019, Nesterova et al., 2019, Pintacuda et al., 2017). We therefore tested whether H4K20me1 enrichment at the Xi is also dependent on the B and C regions of *Xist* RNA. To this end we employed previously established male ESC lines harbouring a DOX inducible, endogenous *Xist* in either its full length form (*XistFL*) or lacking the B and C repeat

regions (*XistΔBC*) (**Fig. 5D**), in which H3K27me3 changes on the Xi had already been mapped (Bousard et al., 2019). This system recapitulates hallmarks of XCI, namely chromosome-wide *Xist* coating, X-linked gene silencing, and heterochromatin formation (Bousard et al., 2019). After DOX treatment we performed IF/RNA FISH experiments to quantify the efficiency of H4K20me1 enrichment at the *Xist* RNA domains (**Fig. 5E**). While the global level of H4K20me1 was comparable in both cell lines it showed, as predicted, striking variability between cells due to different cell cycle stages. Nevertheless, we observed complete loss of H4K20me1 enrichment from the *Xist* RNA domains when *XistΔBC* was expressed; a result reminiscent of what was previously observed for H3K27me3 (**Fig. 4F**) (Bousard et al., 2019). This data indicates that H4K20me1 enrichment depends on the same regions of *Xist* RNA that are involved in recruiting PRC1 and lead to subsequent PRC2 recruitment. Which factors directly target H4K20me1 to the Xi still remains unclear however. Another important conclusion from this result pertains to gene silencing. Indeed, the *XistΔBC* RNA is able to initiate gene silencing, albeit at slightly lower efficiency (Bousard et al., 2019). This implies that the de novo accumulation of H4K20me1 is largely dispensable for the initiation of gene silencing, similarly to both Polycomb-associated H3K27me3 and H2AK119Ub.

Discussion

We report the spatio-temporal dynamics of two early chromatin changes, H4K20me1 and H3K27me3 during the formation of facultative heterochromatin in XCI. Using a unique combination of live-cell imaging and chromatin profiling in the same cell systems, we reveal the relative timing and distributions of chromatin enrichment for these marks during X inactivation. Our study provides insights into the process of XCI and new tools for the study of epigenetic processes in general. Indeed we use the powerful technology of mintbodies, genetically encoded fluorescent probes that can detect specific proteins and their modifications. In this way we visualise the distribution and levels of specific histone modifications, in longitudinal single-cell analyses of the epigenetic process of XCI. We previously reported on the development of mintbodies specific for H4K20me1 and H3K9ac (Sato et al., 2016, Sato et al., 2013). The H3K27me3 mintbody developed here will enable the study of PRC2-dependent epigenetic mechanisms beyond XCI.

Our results reveal that the enrichment of both H3K27me3 and H4K20me1 on the *Xist*-coated chromosome occurs about 45 min following *Xist* RNA coating. This suggests that both marks are deposited on the Xi in a *Xist*-dependent but likely indirect mechanism. It should be noted that proteins such as SPEN which are recruited directly by *Xist* RNA (Chu, Zhang et al., 2015, McHugh et al., 2015, Minajigi, Froberg et al., 2015) show immediate colocalization with *Xist* during initiation of XCI based on live cell imaging using the same ESC system (Dossin et al., 2020). While the initial recruitment of both H4K20me1 and H3K27me3 follows similar dynamics they soon diverge with H3K27me3 accumulating more efficiently. What is more, H4K20me1 shows a unique cell-cycle dynamics with transiently increased levels during G2/M (Rice, Nishioka et al., 2002). In line with these differences our nChIP-seq analysis revealed that both marks also show distinct genomic distribution especially in the context of initially active genes. Thus, while accumulation of both marks depends on a common *Xist*-mediated mechanism their spreading and long term enrichment is regulated independently.

Here we reveal that both H3K27me3 and H4K20me1 accumulation depends on the *Xist* B + C region (Bousard et al., 2019). However, neither SETD8 nor PRC2 core components have identified as direct *Xist* RNA binding proteins (Chu et al., 2015, McHugh et al., 2015, Minajigi et al., 2015). Instead PRC1 is thought to be recruited by this region via the hnRNPK factor. Furthermore SETD8 does not interact with any of the five proteins, including hnRNPK,

recently identified to bind with the *Xist* B+C repeats (Bousard et al., 2019). It thus remains unclear how SETD8, if at all, is recruited to the Xi and whether it depends on the non-canonical PRC1 complexes, as proposed for PRC2 (Almeida et al., 2017, Pintacuda et al., 2017). Indeed, PRC2 recruitment depends on the non-canonical PRC1, which very rapidly deposits H2AK119Ub. This modification in turn is proposed to recruit PRC2 via its cofactors e.g. JARID2 (Cooper, Grijzenhout et al., 2016). Whether a similar mechanism mediates H4K20me1 enrichment remains unclear. A factor potentially involved in indirect SETD8 recruitment is a Polycomb-group protein L3MBTL1, which is not however a cofactor of either PRC1 or PRC2. L3MBTL1 is a binder of H4K20me1 (Kalakonda, Fischle et al., 2008) but it also interacts with SETD8 and H3K27me1/2 (Kalakonda et al., 2008). Thus L3MBTL1 may recruit SETD8, when H3K27 starts to become methylated by PRC2 but the H3K27me1/2 enrichment during XCI has not yet been studied. Alternatively, it is possible that SETD8 is not recruited to the Xi, instead it could be the enzymes catalysing H4K20me2/3 demethylation to H4K20me1, which become enriched during XCI. Indeed, in *Caenorhabditis elegans* dosage compensation, which consists of a reduction of X-linked gene activity in XX individuals, is partly dependent on an H4K20me2-specific demethylase (Brejc et al., 2017). In this system, efficient conversion of H4K20me2 to H4K20me1 at the X chromosome by DPY-21 promotes gene silencing during the maintenance phase. RSBN1 and RSBN1L are mouse orthologs of DPY-21 and seem to retain specific histone demethylase activity (Brejc et al., 2017). Whether RSBN1/RSBN1L have a role in H4K20 methylation dynamics in mammalian cells and whether these factors play a role in XCI merits further investigation.

Identifying the B and C repeats of *Xist* RNA as the key region for H4K20me1 enrichment during XCI suggests that this mark may only play a minor role in initiating gene silencing. Indeed, cells expressing *Xist:ΔBC* can induce X-chromosome gene silencing during XCI albeit with lower efficiency (Bousard et al., 2019). The fact that H4K20me1 is highly enriched at transcribed gene bodies both on the X chromosome (before XCI) and autosomes would also suggest that this mark is not involved in transcriptional repression. Indeed, previous studies reported a positive correlation between H4K20me1 enrichment and the rate of transcriptional elongation (Veloso et al., 2014). SETD8 was also proposed to facilitate RNA Polymerase II (RNAPII) release from promoters (Kapoor-Vazirani & Vertino, 2014, Nikolaou, Moulos et al., 2017). The initial distribution of H4K20me1 is in line with such findings. However this mark also persists at genes which become rapidly silenced during XCI *e.g. Rnf12* (**Fig. 5A**). Thus, transcriptional silencing does not result in rapid H4K20me1 depletion at gene bodies indicating that SETD8 is not directly recruited by the RNAPII. The fact that H4K20me1 remains in gene bodies even as silencing occurs and that it accumulates in intergenic regions during XCI, suggests that it may play a rather different role. Indeed, such a mark may be coupled both to transcriptional elongation and to gene silencing in the context of XCI, if it plays a role in genome stability and/or chromatin structure (Schotta, Sengupta et al., 2008), rather than in gene transcriptional regulation per se.

While H4K20me1 is dispensable for the initiation of gene silencing, it might participate in chromatin compaction during XCI. Indeed, DNA FISH analysis of cells depleted of SETD8 previously revealed some decompaction of the Xi (Oda et al., 2009). The finding that H4K20me1 predominantly accumulates intergenically upon *Xist* induction might support this conclusion. Consistently, in *C. elegans* loss of H4K20me1 enrichment at the X chromosome leads to a decrease in long-range interactions, suggesting impaired chromatin compaction (Brejc et al., 2017). How H4K20me1 might mediate such a process is still far from clear. One factor likely to be involved is L3MBTL1, which becomes recruited to H4K20me1-during S-phase (Kalakonda et al., 2008, Trojer, Li et al., 2007). In vitro, L3MBTL1 compacts nucleosomes in a H4K20me1/2-dependent manner (Trojer et al., 2007). However, the involvement of L3MBTL1 in XCI and chromatin compaction remains to be defined.

In conclusion, we have applied a unique combination of mintbodies to track PRC2-dependent H3K27me3 and H4K20me1 in living cells, together with a high resolution ChIP-seq analysis

to define the precise spatio-temporal distribution of these chromatin marks across the X chromosome during the initiation of XCI. Our approach has uncovered that H3K27me3 and H4K20me1 become enriched thanks to the same B+C region of *Xist* RNA but that the subsequent accumulation dynamics of these marks is rather different during XCI. While de novo H4K20me1 enrichment is dispensable for the initiation of gene silencing it might contribute to chromatin compaction during XCI.

Materials and Methods

Data availability

The accession number for the sequencing datasets reported in this paper is GEO: GSE153146.

Cloning variable fragments of H3K27me3-specific antibody and mutagenesis

Mouse hybridoma clone 2E12 was generated and screened by Mab Institute Inc. as described (Kimura et al., 2008). RNA was extracted from cells using TRIzol (Thermo Fisher Scientific) for RNA-seq and de novo transcriptome assembly to determine cDNA sequence encoding the IgG heavy and light chains, according to (Hayashi-Takanaka et al., 2011, Kuniyoshi et al., 2016). To amplify variable regions of heavy (V_H) and light (V_L) chains, PrimeScript II High Fidelity One step RT-PCR Kit (Takara) was used with the following primers: VH_s, CGAATTCGCCATGGCCCAGGTCCAGTTGCAGCAGTCT; VH_as, TGAACCGCCTCCACCTGAGGAGACTGTGAGAGTGGT; VL_s, TCTGGCGGTGGCGGATCGGACATTGTGATGTCACAGTCT; VL_as, TGGATCCGCCCGTTTGATTTCCAGCTTGGTGCCTCC. As described previously (Sato et al., 2013), the heavy and light chains were connected by PCR (7 cycles) using the amplified fragments with the following oligonucleotides to have a flexible linker: LINK primer1, GTCTCCTCAGGTGGAGGCGGTTCAGGCGGAGGTGGCTCTGGCGGTGGCGGATCG; and LINK primer2, CGATCCGCCACCGCCAGAGCCACCTCCGCCTGAACCGCCTCCACCTGAGGAGAC. The resulting scFv fragments were further amplified (20 cycles) using the 5' and 3' primers: scFv primer_s, CTCGAGCTCAAGCTTCGAATTCGCCATGGCCCAGG and scFv primer_as: CATGGTGGCGACCGGTGGATCCGCCCGTTTTATTTCCAG, for cloning into psfGFP-N1 vector (Addgene #54737) digested with EcoRI and BamHI to yield psfGFP-N1-2E12 using In-Fusion (Takara).

Error-prone PCR was performed to make a few amino acid substitutions in the scFv region using psfGFP-N1-2E12 as a template and a set of primers (scFv primer_s and scFv primer_as) with Taq DNA Polymerase (QIAGEN) in the presence of $MnCl_2$ (6 cycles) (Wilson & Keefe, 2000).

Site-directed mutagenesis was performed by inverse PCR using a mutant clone that contained M86L mutation (psfGFP-N1-2E12M86L) as a template with PrimeSTAR HS DNA polymerase (Takara) and primers to introduce M185I substitution: a472t_s, TGTCAGTTGGAGAGAAGGTTACTTTGGCCTGCAAGT; and a472t_as, ACTTGCAGGCCAAAGTAACCTTCTCTCCAACTGACA.

Mintbody expression in HeLa and MC12 cells

HeLa and MC12 cells were described previously (Sato et al., 2016). Transfection was performed using Fugene HD (Promega) or Lipofectamine 2000 (Thermo Fisher Scientific) according to the manufacturer's' instruction. To obtain stably expressing cells, scFv-sfGFP was cloned into PB533A (System Biosciences) and transfected with the transposase expression vector (PB200PA-1; Systems Biosciences). The day after transfection, cells were grown in 1 mg/ml G418 (Nacalai Tesque) for 1-2 weeks, and fluorescent cells were collected

using a cell sorter (SH800; Sony). Single cell clones were obtained by limiting dilution into 96-well plates and microscopic investigation.

For live cell imaging, cells were plated onto a glass-bottom dish (Mat-Tek; P35G-1.5-14-C), or a glass-bottom plate (AGC Techno Glass; 24-well or 96-well) in FluoroBrite DMEM (Thermo Fisher Scientific) containing 10% FCS (Thermo Fisher Scientific) and 1% Glutamine-Penicillin-Streptomycin solution (Sigma-Aldrich). A glass-bottom dish or a plate was set on to a heated stage (Tokai Hit) with a CO_2 control system (Tokken) on an inverted microscope (Nikon Ti-E) or on a confocal system (Nikon Ti-E with Yokogawa CSU-W1 spinning disk or Olympus FV1000) to maintain cells at 37°C under 5% CO_2 atmosphere.

For immunofluorescence, MC12 cells expressing H3K27me3-mintbody (2E12LI-sfGFP) were fixed with 4% formaldehyde (Electron Microscopy Sciences) in 250 mM HEPES-NaOH (pH 7.4; Wako Purechemicals) containing 0.1% Triton X-100 for 10 min at room temperature. Fixed cells were permeabilized with 1% Triton X-100 in PBS for 20 min at room temperature and washed three times with PBS. After blocking with 10% Blocking One-P (Nacalai Tesque) in PBS for 20 min at room temperature, cells were incubated in 2 µg/ml Cy3-conjugated anti-H3K9me3 (CMA318/2F3; Hayashi-Takanaka et al. 2011) and 2 µg/ml Cy5-conjugated anti-H3K27me3 (CMA323/1E7; Hayashi-Takanaka et al. 2011) for 2 h at room temperature. After washing three times with PBS, cells were incubated with 1 µg/ml Hoechst33342 in PBS for 20 minutes at room temperature. Fluorescence images were sequentially collected using an Olympus FV1000 equipped with a 60× PlanApoN (NA 1.40) oil-immersion lens.

Bacterial expression and purification of mintbody

2E12LI-sfGFP was subcloned into pMAL-c5X (New England Biolabs) to obtain an MBP-2E12LI-sfGFP expression vector (pMAL-c5X-2E12LI-mintbody). E. coli ER2523 cells (NEB Express; New England Biolabs) harboring the pMAL-c5X-2E12LI-mintbody plasmid was grown in 2 ml Plus grow medium (Nacalai Tesque) containing 100 µg/ml ampicillin at 26°C overnight. The whole 2 ml overnight culture was added to 50 ml Plus grow medium, and cells were grown at 26°C for 1 h before the addition of 0.1 mM isopropyl-β-d-thiogalactopyranoside (IPTG). Cells were further grown for 8 h at 26°C and collected by centrifugation (4,000×g; 10 min; 4°C), and the pellet was stored at -30°C. After thawing on ice, the pellet was resuspended in 2.5 ml of Column Buffer (20 mM Tris-HCl, pH 8.0, 200 mM NaCl, 1 mM EDTA) and cells were disrupted using a sonicator (Branson; Sonifier 250; Output 1.2, Duty Cycle 30%, 4 min with intervals on ice). After centrifugation (2,000×g; 10 min; 4°C), the supernatant was collected, diluted 7-fold with Column Buffer, and mixed with 200 µl amylose resin (New England Biolabs) that were pre-equilibrated with Column Buffer. After washing with 15 ml Column Buffer. Bound proteins were eluted with 1.5 ml Column Buffer containing 20 mM maltose. To remove MBP moiety, the concentration of eluted MBP-mintbody was adjusted to 1 mg/ml and digested with 30 µg/ml Factor Xa (New England Biolabs) for 24 h. The cleavage was confirmed by 10-20% SDS polyacrylamide gel electrophoresis (SDS-PAGE). After the buffer was replaced with 20 mM sodium phosphate (pH 5.5) buffer containing 25 mM NaCl using a PD MiniTrap G-25 column (GE Healthcare), the digested sample was applied to a HiTrap Q HP column and every 1.5 ml was collected during the application and washing with the same buffer. Fractions containing H3K27me3-mintbody (2E12LI-sfGFP), analyzed by 10-20% SDS-PAGE, were concentrated using an Amicon Ultra filter unit (Merck; 10 k cut-off).

For peptide array analysis, a MODified Histone Array (Active Motif) was blocked for 1 h at room temperature in Blocking One (Nacalai Tesque) and incubated for 3 h with 0.4 µg/ml H3K27me3-mintbody in Can Get Signal (Toyobo). After washing 3 times for 5 min in Tris-buffered saline (20 mM Tris-HCl, pH 8.0, 150 mM NaCl) containing 0.1% Triton X-100 (TBST), the peptide array was incubated for 1 h with horseradish peroxidase-conjugated anti-GFP (Anti-GFP pAb-HRP-DirecT; 1: 2,000 dilution; MBL) and washed 3 times for 10 min

in TBST. Signals were developed using Western Lightning Plus-ECL (PerkinElmer) and detected using a LuminoGraph II (ATTO).

For immunofluorescence, HeLa cells were plated in a 24-well glass bottom plate (IWAKI) and transfected with expression vectors for HaloTag-tagged KDM6B and KDM4D. Twenty-four hours after transfection, the cells were fixed, permeabilized, and blocked as described above. The cells were incubated for 1 h at room temperature with 5 µg/ml H3K27me3-mintbody, 2 µg/ml Alexa Fluor 488-conjugated anti-H3K27me3 (CMA323/1E7), or 2 µg/ml Alexa Fluor 488-conjugated anti-H3K9me3 (CMA318/2F3) in 10% Blocking One P (Nacalai Tesque) containing 1 µg/ml Hoechst33342 and Janelia Fluor 646 HaloTag Ligand (a gift from Luke Lavis). After washing three times with PBS, fluorescence images were sequentially collected using Nikon Ti-E equipped with a 40× PlanApo (NA 0.9) lens. The nuclear intensities of fluorescence signals were quantified using NIS-elements analysis software.

sgRNA-dCas system to label X-linked loci

To search the target microsatellite repeats for dCas9-GFP-mediated genome visualization, we first enumerated the sequences of $N_{20}GG$ and $N_{21}GG$ whose specificities in a chromosome are greater than 19. The specificity of a sequence *s* in chromosome *c* is defined to be the ratio $f_c(s)/1+\sum_{i\neq c} f_i(s)$, where$f_c(s)$ denotes the frequency of *s* in *c*. Since this entails that sequences appearing less than 20 times in all chromosomes are irrelevant, we employed the *k*-mer counting software DSK (version 2.1.0; (Rizk, Lavenier et al., 2013)) to obtain a list of 22- and 23-mers with a copy number >19 on a chromosome. These sequences and their complementary sequences were used as inputs to the alignment software Bowtie (version 1.1.2; (Langmead, Trapnell et al., 2009)) against the FASTA files (GRCm38, Ensembl 84). We next searched for candidate sequences enriched >19 times in less than 1 Mb. Let *R* be a region in *c*, then the frequency of *s* in *R* is $f_c(s)-n_R(s)$ for some integer $n_R(s)$. Therefore, the condition that the specificity of *s* in *R* being >19 results in $n_R(s)\leq(f_c(s)-20\sum_{i\neq c} f_i(s)\ /21$. For sequence *s* that satisfied the criteria, a comprehensive search for connected regions of lengths less than 1Mb containing $f_c(s)-n_R(s)$ alignments of *s* were performed on its Bowtie alignment output. Among the candidates, 32 sequences were experimentally screened.

The expression vectors for sgRNA and dCas9-EGFP were constructed using those obtained from Yolanda Markaki and Heinrich Leonhardt (Anton et al., 2014). pex-A-U6p-sgRNA(F+E)-BbsI was first generated from pEX-A-U6-sgRNA-antiMiS, which contained microsatellite-specific sequence, to clone X-linked sgRNA into the BbsI site. Oligonucleotides consisting of the target sequence and BbsI sites were synthesized (Hokkaido System Science; Supplementary table 1) and annealed to insert into the linearized pex-A-U6p-sgRNA(F+E)-BbsI. Each of the resulting plasmids was co-transfected with dCas9-EGFP expression vector into MC12 cells grown on a 24-well glass-bottom plate (IWAKI) using Liopofecamine 2000 (ThermoFisher Scientific), according to the manufacturer's instruction. Among 32 sgRNA screened, 7 that exhibited distinct spots by transient expression (Supplementary table 1) were subcloned into a piggybac-vector PB510B-1 (System BioSciences) to establish stable lines. dCas9-EGFP was also subcloned into another piggyback vector PB533-A2 (System BioSciences). The resulting PB510B-based sgRNA expression vector and PB533-dCas9-EGFP were co-transfected with a transposase expression vector PB200PA-1 (System BioSciences) into MC12 cells, and stable clones were selected in 1 mg/ml G418 and 1 µg/ml puromycin.

The selected MC12 cell lines were plated on a 35-mm glass bottom dish (IWAKI) and fixed with 4% formaldehyde (Electron Microscopy Sciences) in 250 mM HEPES-NaOH (pH 7.4; Wako Purechemicals) containing 0.1% Triton X-100 for 5 min at room temperature. Fixed cells were permeabilized with 1% Triton X-100 in PBS for 20 min at room temperature and washed three times with PBS. The cells were incubated with 2 µg/ml Cy5-conjugated anti-H3K27me3 (CMA323/1E7; Hayashi-Takanaka et al. 2011) and 1 µg/ml Hoechst33342 in

10% Blocking One P (Nacalai Tesque) in PBS for 1 h at room temperature. After washing three times with PBS, fluorescence images were sequentially collected using a confocal microscope (Nikon Ti-E with Yokogawa CSU-W1 spinning disk and Andor iXon3 EM-CCD).

To obtain mitotic cells, MC12 cells were plated on 35-mm glass bottom dish (IWAKI) and treated with colcemid (Nacalai Tesque) at a final concentration of 50 ng/ml in the medium for 90 min. After removal of the medium, 75 mM KCl was added to the dish and incubated for 30-40 min at room temperature to swell the cells. The mitotic cells were fixed with 250 mM HEPES-NaOH (pH 7.4; Wako Purechemicals) for 5 min at room temperature and permeabilized with 0.1% Triton X-100 in PBS for 20 min at room temperature. After washing with PBS, cells were stained with Cy5-conjugated anti-H3K27me3 and Hoechst33342, as described above.

To visualize X-linked loci simultaneously with H3K27me3 or H4K20me1 during X inactivation, female mESC lines expressing the two sgRNA (mX8 and mX26), 3×sfGFP-dCas9, and H3K27me3-mintbody (mCherry version) and H4K20me1-mintbody (HaloTag version visualized with JF646) were established. For tracking differentiating mouse ESCs in 3D over several hours, we used mintbodies tagged with nuclear localization signals to increase the brightness in nuclei. Therefore, the oscillation of the global modification levels throughout the cell cycle was not monitored (Rice et al., 2002). PGK12.1 mouse female ES cells (Penny et al., 1996) were routinely grown on dish coated with 0.1% gelatin (Wako Purechemicals) in DMEM high glucose (Nacalai Tesque) with 10% FBS (ThermoFisher Scientific), 1% L-Glutamine-Penicillin-Streptomycin Solution (Sigma-Aldrich), 1% MEM nonessential amino acid solution (Nacalai Tesque), 1 mM Sodium Pyruvate (ThermoFisher Scientific), 55 µM 2-mecaptoethanol (ThermoFisher Scientific), 10^3 units/ml leukemia inhibitory factor (LIF; Nacalai Tesque) at 37℃, 5% CO_2 atmosphere. PGK12.1 cells were transfected with the expression vectors using Liopofecamine 2000 (ThermoFisher Scientific) and selected in 1 mg/ml G418 and 1 µg/ml puromycin to obtain stable cell lines. To induce differentiation, cells were plated at 1-2×10^4 cells per 10 cm dish and incubated with LIF-free medium. For live imaging, mESCs were plated on 35-mm µ-Dish (ibidi) coated with laminin (BioLamina) in FluoroBrite DMEM (Thermo Fisher Scientific) containing all the other supplements described above. The fluorescence images were sequentially collected using a confocal system (Nikon Ti-E with Yokogawa CSU-W1 spinning disk and Andor iXon3 EM-CCD) with a heated stage (Tokai Hit) to maintain cells at 37°C under 5% CO_2 atmosphere.

TX based ESC Lines

TX1072 (mouse, female, [*Mus musculus castaneus X* C57BL/6] embryonic stem cells) cells have been previously derived in the lab (Schulz et al., 2014). TX-BglSL cell line has been previously derived from TX1072 (Dossin et al., 2020). TX-Bgl-EGFP was established by targeting a BglG-EGFP expression cassette into the ROSA26 permissive locus. This was done by simultaneously transfecting TX-BglSL ESCs with a targeting vector (ROSA26 homology arms, CAGS promoter and BglG-EGFP-NLS fusion gene) and two pX330 plasmids containing two sgRNAs to ROSA26 (TGGGCGGGAGTCTTCTGGGC and ACTGGAGTTGCAGATCACGA). TX-Bgl-mCherry cell line was derived by targeting BglG-mCherry expression cassette into the TIGRE permissive locus. This was done by simultaneously transfecting TX-BglSL ESCs with a targeting vector (TIGRE homology arms, CAGS promoter and BglG-mCherry-NLS fusion gene) and a single pX459 plasmids containing an sgRNA to TIGRE (ACTGCCATAACACCTAACTT). After brief puromycin selection, clones were picked and screened by imaging. Subsequently, clones with heterozygous insertion of the BglG cassette were selected by genotyping PCR. The TX-Bgl-EGFP; H4K20me1-mCherry cell line was derived by co-transfecting TX-Bgl-EGFP with pBaso transposase vector and a piggyBac vector harbouring an expression cassette for H4K20me1 mintbody (15F11-mCherry) (Sato et al., 2016). The TX-Blg-mCherry; H3K27me3-sfGFP cell line was derived by co-transfecting TX- Blg-mCherry with pBaso transposase

vector and a piggyBac vector harbouring an expression cassette for H3K27me3 mintbody (2E12LI-sfGFP). All TX1072-based ESC lines were cultured on gelatine-coated plates in Dulbecco's Modified Eagle Medium (DMEM) supplemented with 15% foetal bovine serum, 2-mercaptoethanol (0.1mM), LIF(1000U/mL) and 2i (PD0325901 [0.4 mM], CHIR99021 [3 mM]). Cells were incubated at 37°C with 8% CO_2.
TXY:*XistFL* (mouse, male embryonic stem cells) were obtained from the Wutz team (Wutz et al., 2002) and TXY:*XistΔBC* was previously derived in the lab (Bousard et al., 2019). These lines were cultured on gelatine-coated plates in Dulbecco's Modified Eagle Medium (DMEM) supplemented with 15% fetal bovine serum, 2-mercaptoethanol (50mM) and LIF (1000U/mL). Cells were incubated at 37°C with 8% CO_2.

DOX treatment
For TX1072-based ESC lines after 24hrs of culture in DMEM/15%FCS+LIF+2i the medium was supplemented with doxycycline (1µg/ml). For TXY based ESC lines after 24hrs of culture in DMEM/15%FCS+LIF cells were washed twice with PBS and medium was changed to DMEM/10%FCS-LIF with doxycycline (1.5µg/ml). Cells were collected after 48hrs of differentiation.

Antibody validation
H3K27me3 mintbody and H4K20me1 antibody used for nChIP-seq (Active Motif cat. 39727) were validated for sensitivity and specificity using the MODified Histone Peptide Array (ActiveMotif) following manufacturer's instructions.

Native ChIP-seq
Native ChIP-seq was performed as previously described (Zylicz et al., 2019). Cells were collected using Accutase (Thermo Fisher Scientific), washed twice in ice-cold PBS and counted. Typically, 10 million (mln) cells were used per immunoprecipitation (IP). A fraction of cells was always used for RNA/FISH verification of *Xist* induction. Cell pellet was resuspended in 90 µL (per 10 mln cells) of Lysis Buffer (50 mM Tris-HCl, pH7.5; 150mM NaCl; 0.1% sodium deoxycholate; 1% Triton X-100; 5mM $CaCl_2$; Protease Inhibitor Cocktail (Roche); 5 mM sodium butyrate). After lysing cells on ice for 10 min we added 62 µL (per 10 mln cells) of Lysis Buffer with MNase (500 µL buffer + 0.5 µL MNase). Chromatin was digested for exactly 8 min at 37°C and reaction was stopped by the addition of 20 mM EGTA. To remove undigested debris the lysates were centrifuged at 13000 rpm for 5 min at 4°C. Supernatant was transferred to a fresh tube, an equal volume of STOP Buffer (50 mM Tris-HCl, pH7.5; 150mM NaCl; 0.1% sodium deoxycholate; 1% Triton X-100; 30 mM EGTA; 30 mM EDTA; Protease Inhibitor Cocktail; 5 mM sodium butyrate) was added, and samples were stored on ice. For the nChIP input, 5 µL of lysate was digested in 45 µL of ProtK Digestion Buffer (20 mM HEPES; 1 mM EDTA; 0.5% SDS, 0.8 mg/ml Proteinase K) for 30 min at 56°C. 50 µL of AMPure XP beads were added to the digested lysate together with 60 µL of 20% PEG8000 1.25M NaCl. After mixing the samples were incubated for 15 min at RT. Beads were separated on a magnet and washed twice with 80% ethanol for 30 sec. DNA was eluted in 12 µL of Low-EDTA TE. DNA isolated in this step was used as the input sample. The volume of each undigested lysate was adjusted to obtain 1mL per IP using a 1:1 mix of Lysis Buffer and STOP Buffer. Anti-mouse Dynabeads (25µl/IP) were washed twice in Blocking Buffer (0.5% BSA; 0.5% Tween in PBS). Beads were then resuspended in Blocking buffer and coated with antibodies for 4 hrs at 4°C (H4K20me1 [0.5 µg/IP], Active Motif cat. 39727). Once coated beads were magnet-separated and resuspended in 1 mL of lysate. Samples were left rotating overnight at 4°C. Following day beads were magnet-separated and washed quickly with ice-cold washing buffers: 4-times with Low Salt Buffer, 2-times with High Salt Buffer (0.1% SDS; 1% Triton X-100; 2 mM EDTA; 20 mM Tris-HCl, pH 8.1; 360 mM NaCl; 0.1% sodium deoxycholate) and 2-times with LiCl buffer (0.25 M LiCl; 1% NP40;1.1% sodium deoxycholate; 1 mM EDTA; 10 mM Tris-HCl pH 8.1). Prior to elution all samples were rinsed once in TE. ChIP-DNA was eluted in ProtK-Digestion buffer for 15 min

at 56°C. Beads were separated and the supernatant was further digested for another 2 hr at 56°C. DNA was isolated using AMPure XP beads as described for the input sample.
For each nChIP-seq, 0.5 µL of each sample was used for qPCR validation of enrichment at control regions. 0.5 µL of input samples were also used to verify the digestion efficiency using D1000 tapestation. Remaining DNA concentration was adjusted and used for library preparation using Ovation® Ultralow Library System V2 following suppliers protocol. Amplified libraries were size-selected for dinucleotide fraction (350-600bp fragments) using agarose gel-separation and MinElute Gel Extraction Kit (QIAGEN). Sample quality was inspected using D1000 tapestation. Samples were sequenced using a HiSeq2500 with Paired-End (PE) 100 or a HiSeq4000 PE150.

nChIP-seq Data processing
Adapters and low quality bases (< Q20) have been removed with TrimGalore (v0.4.4; http://www.bioinformatics.babraham.ac.uk/projects/trim_galore) and Cutadapt (1.12) (Martin, 2011). Moreover, for PE150 samples, last 50 pb were trimmed to allow unbiased comparison of the data with PE100 samples. An 'N-masked" genome has been generated with SNPSplit (0.3.2) (Krueger & Andrews, 2016) which is a version of the mouse reference genome mm10 where all the polymorphic sites for the hybrid strain *Mus musculus* CAST/EiJ and *Mus musculus* C57BL/6 are masked by ambiguity nucleobase 'N'. For all samples, reads were then mapped to the 'N-masked" genome with STAR (2.5.3a) with options [--outFilterMultimapNmax 1 --outSAMmultNmax 1 --outFilterMismatchNmax 999 --outFilterMismatchNoverLmax 0.03 --alignIntronMax 1 --alignEndsType EndToEnd --outSAMattributes NH HI NM MD] (Dobin, Davis et al., 2013). Duplicates were discarded with Picard MarkDuplicates (1.65) with options [REMOVE_DUPLICATES = true] (https://broadinstitute.github.io/picard/) and reads mapped on blacklisted regions from Encode Consortium were discarded. SNPSplit (0.3.2) (Krueger & Andrews, 2016) was then used to generate allele-specific BAM files by separating the alignment into two distinct alleles (CAST and B6) based on SNPs information downloaded from Sanger. Bigwig files were created with bedtools genome CoverageBed (2.27.1) (Quinlan & Hall, 2010), using a scale factor calculated on the total library (10.000.000/total reads) for both allele specific bigwigs, and loaded on UCSC genome browser. H3K27me3 nChIP-seq data was downloaded from GSE116990 and processed identically to H4K20me1 nChIP-seq.

Windows definition
Global analysis was first done on fixed windows (10 kb) spanning the whole genome, then on different genomic subcategories: initially active genes, silent genes and intergenic regions. Initially active genes were defined as genes with a transcript having its TSS (refFlat annotation) overlapping a consensus peak of H3K9ac and a consensus peak of H3K4me3. Moreover, initially active genes were filtered to remove potentially bivalent genes by discarding genes with a normalized H3K27me3 signal superior to 0.035 at t0, value defined from the intersection of density curves of H3K27me3 premarking signal of genes initially defined as active and inactive. For genes having several active transcripts detected, the active gene was defined as starting at the minimum start of transcripts, and ending at the maximum end of transcripts. Moreover, using RNA-seq data (Zylicz et al., 2019), genes having a mean TPM (2 samples) < 1 at t0 were excluded from this list. Silent genes were defined as genes with TSS not overlapping a consensus peak of H3K9ac and a consensus peak of H3K4me3. Using RNA-seq data (ref), genes having a mean TPM > 1 at t0 were excluded from this list. Intergenic regions were defined as 10 kb windows not overlapping a gene (active or inactive) and its promoter (2kb upstream) or an active enhancer (defined in (Zylicz et al., 2019).

Counts and normalisation
For all defined windows, total and allelic reads overlapping those features were then counted using featureCounts (1.5.1), with options [-C -p -P] (Liao, Smyth et al., 2014). Then, analysis

was done based on normalized reads from B6 allele (allele of the inactive X chromosome). For each sample, a normalization factor was calculated with the trimmed mean of M-values method (TMM) from edgeR package (Robinson, McCarthy et al., 2010), based on B6 reads overlapping consensus peaks located on autosomes. Peaks of each sample were first identified using MACS2 (2.0.10) with -B --broad options. For each replicate, all peaks coordinates were merged using bedtools merge (2.27.1) (Quinlan & Hall, 2010). Then, common regions between merged peaks coordinates of each replicate were selected using bedtools intersectBed (2.27.1) (Quinlan & Hall, 2010) to represent B6 read accumulation compared to time 0, subtraction of normalised initial counts (time 0) was then applied to all other time points.

Analysis of the dynamics

Sigmoidal fitting of B6 read accumulation in function of time has also been done with the four-parameter log-logistic function from drc R package. Sigmoidal fittings with low residuals (< mean(residuals) + 1.5 sd(residuals)) were selected. The ED_{50} of the sigmoidal fitting were calculated for each window. Windows with ED_{50} derivative superior to 24h, or not calculated, were considered as windows with a late accumulation of repressive marks, those were then replaced by 24h. For pairwise comparison between marks, only windows with ED_{50} inferior to 24h for both marks were selected.

Average plots over features

Average plots were created around initially active and silent genes using DeepTools (3.0.2) (Ramirez, Dundar et al., 2014). Matrix counts were created using DeepTools computeMatrix around genes(see above) on chrX and autosomes separately (with option [--binSize 500]), plots were then created using DeepTools PlotProfile.

Average plots were created with same method around early and late silenced genes. Those genes were defined with a 3 clusters k-means based on IC35 values calculated after sigmoidal fitting of TT-seq data such as described in (Zylicz et al., 2019), defining early, intermediate and late silenced genes.

IF/RNA FISH

IF/RNA FISH experiments were performed as previously (Bousard et al., 2019). *Xist* FL and mutant ES cells were differentiated for 48 h in the presence of DOX (1.5 µg/ml) on gelatine coated 22 × 22 mm coverslips. Cells were fixed in 3% PFA in PBS for 10 min at RT, followed by permeabilization in PBS containing 0.5% Triton X 100 and ribonucleoside-vanadyl complex (New England Biolabs) on ice for 5 min. After three rapid washes in PBS, samples were blocked for, at least, 15 min with 5% gelatine from cold water fish skin (Sigma) in PBS. Coverslips were incubated with the H4K20me1 primary antibody (Abcam, abb9051) diluted in blocking solution in the presence of a ribonuclease inhibitor (0.8 µl/ml; Euromedex) for 45 min at RT. After three washes with PBS for 5 min, the coverslips were incubated with a secondary antibody (anti rabbit antibodies conjugated with Alexa fluorophores diluted 1:500) for 45 min in blocking solution supplemented with ribonuclease inhibitor (0.8 µl/ml; Euromedex). Coverslips were then washed three times with PBS for 5 min at RT. Afterwards, cells were post-fixed with 3% PFA in PBS for 10 min at RT and rinsed three times in PBS and twice in 2× SSC. Excess of 2× SSC was removed, and cells were hybridized with a *Xist* p510 probe labelled with Alexa labelled dUTPs. After the RNA FISH procedure, nuclei were stained with DAPI (Sigma Aldrich), diluted 1:5,000 in 2× SCC for 5 min at RT, and mounted with Vectashield Mounting Medium (Vectorlabs). Cells were imaged with a widefield fluorescence microscope Zeiss Axio Observer (Carl Zeiss MicroImaging) with a 63× oil objective using the filter sets FS43HE, FS38HE, FS50, and FS49. Digital images were analysed with the FIJI platform (https://fiji.sc/). Enrichment of the H4K20me1 signals over *Xist* cloud marked by RNA FISH was counted from at least 50 cells per single experiment.

RNA extraction, reverse transcription, pyrosequencing

RNA was extracted according to the manufacturer's recommendations using RNeasy Mini Kit (QIAGEN) with on-column DNase digestion (QIAGEN). For cDNA synthesis 1.1 µg RNA was reverse transcribed using Superscript III Reverse Transcriptase (Thermo Fisher Scientific). For allelic-skewing analysis the cDNA was PCR-amplified with biotinylated primers and sequenced using the Pyromark Q24 system (QIAGEN).

Live-cell imaging of TX1072-based ESC lines

For all TX1072-based ESC lines one day before imaging, 30,000 cells were seeded in a fibronectin coated µ-Slide 8 well with glass bottom (Ibidi) in 300 µl medium. To induce *Xist* expression, doxycycline was added to medium 5 min before imaging. Live-cell imaging was performed on an inverted spinning disk confocal microscope Roper/Nikon using a Evolve EM-CCD camera (Photometrics) with a 60× oil objective. Images were taken every 15 minutes for 10 hours with Z slices with 400 nm intervals. During imaging cells were kept in a chamber at 37°C and 5% CO2.

Quantification of mintbody accumulation was performed using Icy Version 1.9.8.1 and ImageJ. Quantification was done on maximum projections of z-planes. The TX-Bgl-EGFP or TX-Bgl-mCherry channel was segmented into an *Xist*-enriched region to separate the Xi from the rest of the nucleus. This region was then applied to the mintbody channel and mean intensity of the signal was measured per time point. To normalise for the background signal in the nucleus, every 10 time points the signal in the same nucleus was measured using ImageJ. This was used to calculate the background for every time point. The value of signal in the cloud was then divided by this background.

Acknowledgements

We are grateful to members of the Heard Lab (Curie Institute and EMBL Heidelberg), especially Francois Dossin, for their help and critical input to this project. We also want to thank the Bioimaging facility at iMM JLA for their technical support with fluorescent light microscopy and imaging analysis, and the Biomaterials Analysis Division, Open Facility Center, Tokyo Institute of Technology for DNA sequencing analysis. We thank Yolanda Markaki and Heinrich Leonhardt (LMU Munich) for sgRNA-dCas9 plasmid constructs. This work was supported by Fundac□ão para a Cie□ncia e Tecnologia (S.T.d.R), project grants PTDC/BIA- MOL/29320/2017 IC&DT (A. C. R. & S.T.d.R), CEECUIND/01234/207 (S.T.d.R), and SFRH/BD/137099/2018 (A.C.R.), by an ERC Advanced Investigator award ERC-ADG-2014 671027 attributed to E.H., Sir Henry Wellcome Postdoctoral Fellowship (J.J.Z.), Japan Society for the Promotion of Science KAKENHI grants (JP17KK0143 and JP20K06484 to Y.S., JP19H04970, JP19H03158 and JP20H05393 to K.M., JP18H05532 to H.Ku, JP18H05527 and JP20H00456 to Y.O., JP17H01417 and JP18H05527 to H.Ki), and Japan Science and Technology Agency (JST) CREST JPMJCR16G1 to T.K., H.Ku, Y.O. and H.Ki. J.J.Z. is supported by core funding of The Novo Nordisk Foundation Center for Stem Cell Biology (Novo Nordisk Foundation grant number NNF17CC0027852)

Author contributions

Conceptualization: J.J.Z, E.H., H.Ki.; Methodology: S.T., J.R., A.L.S, M.H., A.O.; Software: J.N.; Validation: S.T., M.H., K.M.; Formal analysis: S.T., A.B., J.J.Z, T.K.; Investigation: S.T., J.J.Z, A.C.R, M.H., Y.S., A.O; Resources: A.L.S, J.N.; Data Curation: A.B.; Writing – original draft preparation: J.J.Z, Y.S., H.Ki.; Writing – review and editing: S.T., A.B., S.T.d.R, E.H.; Visualization: S.T., A.B., J.J.Z, S.T.d.R, M.H., Y.S.; Supervision: J.J.Z, E.H., S.T.d.R, Y.S., Y.O., H.Ku, H.Ki.; Project administration: J.J.Z, Y.S., H.Ki., E.H.; Funding acquisition: J.J.Z, E.H., H.Ki.

Conflict of interest

The authors declare no competing interests.

References

Abe K, Takagi N, Sasaki M (1988) Nonhistone nuclear proteins specific to certain mouse embryonal carcinoma clones having an inactive X chromosome. *Exp Cell Res* 179: 590-4

Almeida M, Pintacuda G, Masui O, Koseki Y, Gdula M, Cerase A, Brown D, Mould A, Innocent C, Nakayama M, Schermelleh L, Nesterova TB, Koseki H, Brockdorff N (2017) PCGF3/5-PRC1 initiates Polycomb recruitment in X chromosome inactivation. *Science* 356: 1081-1084

Anton T, Bultmann S, Leonhardt H, Markaki Y (2014) Visualization of specific DNA sequences in living mouse embryonic stem cells with a programmable fluorescent CRISPR/Cas system. *Nucleus* 5: 163-72

Arai R, Sugawara T, Sato Y, Minakuchi Y, Toyoda A, Nabeshima K, Kimura H, Kimura A (2017) Reduction in chromosome mobility accompanies nuclear organization during early embryogenesis in Caenorhabditis elegans. *Sci Rep* 7: 3631

Beck DB, Oda H, Shen SS, Reinberg D (2012) PR-Set7 and H4K20me1: at the crossroads of genome integrity, cell cycle, chromosome condensation, and transcription. *Genes Dev* 26: 325-37

Blackledge NP, Farcas AM, Kondo T, King HW, McGouran JF, Hanssen LL, Ito S, Cooper S, Kondo K, Koseki Y, Ishikura T, Long HK, Sheahan TW, Brockdorff N, Kessler BM, Koseki H, Klose RJ (2014) Variant PRC1 complex-dependent H2A ubiquitylation drives PRC2 recruitment and polycomb domain formation. *Cell* 157: 1445-59

Bousard A, Raposo AC, Żylicz JJ, Picard C, Pires VB, Qi Y, Gil C, Syx L, Chang HY, Heard E, da Rocha ST (2019) The role of Xist-mediated Polycomb recruitment in the initiation of X-chromosome inactivation. *EMBO reports*

Brejc K, Bian Q, Uzawa S, Wheeler BS, Anderson EC, King DS, Kranzusch PJ, Preston CG, Meyer BJ (2017) Dynamic Control of X Chromosome Conformation and Repression by a Histone H4K20 Demethylase. *Cell* 171: 85-102 e23

Calabrese JM, Sun W, Song L, Mugford JW, Williams L, Yee D, Starmer J, Mieczkowski P, Crawford GE, Magnuson T (2012) Site-specific silencing of regulatory elements as a mechanism of X inactivation. *Cell* 151: 951-63

Cattaneo A, Biocca S (1999) The selection of intracellular antibodies. *Trends Biotechnol* 17: 115-21

Chandra T, Kirschner K, Thuret JY, Pope BD, Ryba T, Newman S, Ahmed K, Samarajiwa SA, Salama R, Carroll T, Stark R, Janky R, Narita M, Xue L, Chicas A, Nunez S, Janknecht R, Hayashi-Takanaka Y, Wilson MD, Marshall A et al. (2012) Independence of repressive histone marks and chromatin compaction during senescent heterochromatic layer formation. *Mol Cell* 47: 203-14

Chen B, Gilbert LA, Cimini BA, Schnitzbauer J, Zhang W, Li GW, Park J, Blackburn EH, Weissman JS, Qi LS, Huang B (2013) Dynamic imaging of genomic loci in living human cells by an optimized CRISPR/Cas system. *Cell* 155: 1479-91

Chu C, Zhang QC, da Rocha ST, Flynn RA, Bharadwaj M, Calabrese JM, Magnuson T, Heard E, Chang HY (2015) Systematic discovery of Xist RNA binding proteins. *Cell* 161: 404-16

Colognori D, Sunwoo H, Kriz AJ, Wang CY, Lee JT (2019) Xist Deletional Analysis Reveals an Interdependency between Xist RNA and Polycomb Complexes for Spreading along the Inactive X. *Mol Cell* 74: 101-117 e10

Cooper S, Grijzenhout A, Underwood E, Ancelin K, Zhang T, Nesterova TB, Anil-Kirmizitas B, Bassett A, Kooistra SM, Agger K, Helin K, Heard E, Brockdorff N (2016) Jarid2 binds

mono-ubiquitylated H2A lysine 119 to mediate crosstalk between Polycomb complexes PRC1 and PRC2. *Nat Commun* 7: 13661
de Napoles M, Mermoud JE, Wakao R, Tang YA, Endoh M, Appanah R, Nesterova TB, Silva J, Otte AP, Vidal M, Koseki H, Brockdorff N (2004) Polycomb group proteins Ring1A/B link ubiquitylation of histone H2A to heritable gene silencing and X inactivation. *Dev Cell* 7: 663-76
Dobin A, Davis CA, Schlesinger F, Drenkow J, Zaleski C, Jha S, Batut P, Chaisson M, Gingeras TR (2013) STAR: ultrafast universal RNA-seq aligner. *Bioinformatics* 29: 15-21
Dossin F, Pinheiro I, Zylicz JJ, Roensch J, Collombet S, Le Saux A, Chelmicki T, Attia M, Kapoor V, Zhan Y, Dingli F, Loew D, Mercher T, Dekker J, Heard E (2020) SPEN integrates transcriptional and epigenetic control of X-inactivation. *Nature* 578: 455-460
Ewert S, Honegger A, Pluckthun A (2004) Stability improvement of antibodies for extracellular and intracellular applications: CDR grafting to stable frameworks and structure-based framework engineering. *Methods* 34: 184-99
Hayashi-Takanaka Y, Yamagata K, Wakayama T, Stasevich TJ, Kainuma T, Tsurimoto T, Tachibana M, Shinkai Y, Kurumizaka H, Nozaki N, Kimura H (2011) Tracking epigenetic histone modifications in single cells using Fab-based live endogenous modification labeling. *Nucleic Acids Res* 39: 6475-88
Hori T, Shang WH, Toyoda A, Misu S, Monma N, Ikeo K, Molina O, Vargiu G, Fujiyama A, Kimura H, Earnshaw WC, Fukagawa T (2014) Histone H4 Lys 20 monomethylation of the CENP-A nucleosome is essential for kinetochore assembly. *Dev Cell* 29: 740-9
Jambhekar A, Dhall A, Shi Y (2019) Roles and regulation of histone methylation in animal development. *Nat Rev Mol Cell Biol* 20: 625-641
Kalakonda N, Fischle W, Boccuni P, Gurvich N, Hoya-Arias R, Zhao X, Miyata Y, Macgrogan D, Zhang J, Sims JK, Rice JC, Nimer SD (2008) Histone H4 lysine 20 monomethylation promotes transcriptional repression by L3MBTL1. *Oncogene* 27: 4293-304
Kalantry S, Mills KC, Yee D, Otte AP, Panning B, Magnuson T (2006) The Polycomb group protein Eed protects the inactive X-chromosome from differentiation-induced reactivation. *Nat Cell Biol* 8: 195-202
Kapoor-Vazirani P, Vertino PM (2014) A dual role for the histone methyltransferase PR-SET7/SETD8 and histone H4 lysine 20 monomethylation in the local regulation of RNA polymerase II pausing. *J Biol Chem* 289: 7425-37
Kimura H (2013) Histone modifications for human epigenome analysis. *J Hum Genet* 58: 439-45
Kimura H, Hayashi-Takanaka Y, Goto Y, Takizawa N, Nozaki N (2008) The organization of histone H3 modifications as revealed by a panel of specific monoclonal antibodies. *Cell Struct Funct* 33: 61-73
Kohlmaier A, Savarese F, Lachner M, Martens J, Jenuwein T, Wutz A (2004) A chromosomal memory triggered by Xist regulates histone methylation in X inactivation. *PLoS Biol* 2: E171
Krueger F, Andrews S (2016) *SNPsplit: Allele-specific splitting of alignments between genomes with known SNP genotypes [version 2; referees: 3 approved]*.
Kuniyoshi Y, Maehara K, Iwasaki T, Hayashi M, Semba Y, Fujita M, Sato Y, Kimura H, Harada A, Ohkawa Y (2016) Identification of Immunoglobulin Gene Sequences from a Small Read Number of mRNA-Seq Using Hybridomas. *PLoS One* 11: e0165473
Langmead B, Trapnell C, Pop M, Salzberg SL (2009) Ultrafast and memory-efficient alignment of short DNA sequences to the human genome. *Genome Biol* 10: R25
Leem J, Dunbar J, Georges G, Shi J, Deane CM (2016) ABodyBuilder: Automated antibody structure prediction with data-driven accuracy estimation. *MAbs* 8: 1259-1268
Liao Y, Smyth GK, Shi W (2014) featureCounts: an efficient general purpose program for assigning sequence reads to genomic features. *Bioinformatics* 30: 923-30
Lim HJ, Dimova NV, Tan MK, Sigoillot FD, King RW, Shi Y (2013) The G2/M regulator histone demethylase PHF8 is targeted for degradation by the anaphase-promoting complex containing CDC20. *Mol Cell Biol* 33: 4166-80
Lyon MF (1962) Sex chromatin and gene action in the mammalian X-chromosome. *Am J Hum Genet* 14: 135-48

Ma H, Naseri A, Reyes-Gutierrez P, Wolfe SA, Zhang S, Pederson T (2015) Multicolor CRISPR labeling of chromosomal loci in human cells. *Proc Natl Acad Sci U S A* 112: 3002-7
Martin M (2011) Cutadapt removes adapter sequences from high-throughput sequencing reads. *2011* 17
Masui O, Heard E, Koseki H (2018) Live Imaging of Xist RNA. *Methods Mol Biol* 1861: 67-72
McHugh CA, Chen CK, Chow A, Surka CF, Tran C, McDonel P, Pandya-Jones A, Blanco M, Burghard C, Moradian A, Sweredoski MJ, Shishkin AA, Su J, Lander ES, Hess S, Plath K, Guttman M (2015) The Xist lncRNA interacts directly with SHARP to silence transcription through HDAC3. *Nature* 521: 232-6
Minajigi A, Froberg JE, Wei C, Sunwoo H, Kesner B, Colognori D, Lessing D, Payer B, Boukhali M, Haas W, Lee JT (2015) Chromosomes. A comprehensive Xist interactome reveals cohesin repulsion and an RNA-directed chromosome conformation. *Science* 349
Nesterova TB, Wei G, Coker H, Pintacuda G, Bowness JS, Zhang T, Almeida M, Bloechl B, Moindrot B, Carter EJ, Alvarez Rodrigo I, Pan Q, Bi Y, Song CX, Brockdorff N (2019) Systematic allelic analysis defines the interplay of key pathways in X chromosome inactivation. *Nat Commun* 10: 3129
Nikolaou KC, Moulos P, Harokopos V, Chalepakis G, Talianidis I (2017) Kmt5a Controls Hepatic Metabolic Pathways by Facilitating RNA Pol II Release from Promoter-Proximal Regions. *Cell Rep* 20: 909-922
Nishioka K, Rice JC, Sarma K, Erdjument-Bromage H, Werner J, Wang Y, Chuikov S, Valenzuela P, Tempst P, Steward R, Lis JT, Allis CD, Reinberg D (2002) PR-Set7 is a nucleosome-specific methyltransferase that modifies lysine 20 of histone H4 and is associated with silent chromatin. *Mol Cell* 9: 1201-13
Oda H, Okamoto I, Murphy N, Chu J, Price SM, Shen MM, Torres-Padilla ME, Heard E, Reinberg D (2009) Monomethylation of histone H4-lysine 20 is involved in chromosome structure and stability and is essential for mouse development. *Mol Cell Biol* 29: 2278-95
Penny GD, Kay GF, Sheardown SA, Rastan S, Brockdorff N (1996) Requirement for Xist in X chromosome inactivation. *Nature* 379: 131-7
Pintacuda G, Wei G, Roustan C, Kirmizitas BA, Solcan N, Cerase A, Castello A, Mohammed S, Moindrot B, Nesterova TB, Brockdorff N (2017) hnRNPK Recruits PCGF3/5-PRC1 to the Xist RNA B-Repeat to Establish Polycomb-Mediated Chromosomal Silencing. *Mol Cell* 68: 955-969 e10
Pinter SF, Sadreyev RI, Yildirim E, Jeon Y, Ohsumi TK, Borowsky M, Lee JT (2012) Spreading of X chromosome inactivation via a hierarchy of defined Polycomb stations. *Genome Res* 22: 1864-76
Plath K, Fang J, Mlynarczyk-Evans SK, Cao R, Worringer KA, Wang H, de la Cruz CC, Otte AP, Panning B, Zhang Y (2003) Role of histone H3 lysine 27 methylation in X inactivation. *Science* 300: 131-5
Quinlan AR, Hall IM (2010) BEDTools: a flexible suite of utilities for comparing genomic features. *Bioinformatics* 26: 841-2
Ramirez F, Dundar F, Diehl S, Gruning BA, Manke T (2014) deepTools: a flexible platform for exploring deep-sequencing data. *Nucleic Acids Res* 42: W187-91
Rastan S, Robertson EJ (1985) X-chromosome deletions in embryo-derived (EK) cell lines associated with lack of X-chromosome inactivation. *Journal of Embryology and Experimental Morphology* 90: 379-388
Rice JC, Nishioka K, Sarma K, Steward R, Reinberg D, Allis CD (2002) Mitotic-specific methylation of histone H4 Lys 20 follows increased PR-Set7 expression and its localization to mitotic chromosomes. *Genes Dev* 16: 2225-30
Rizk G, Lavenier D, Chikhi R (2013) DSK: k-mer counting with very low memory usage. *Bioinformatics* 29: 652-3
Robinson MD, McCarthy DJ, Smyth GK (2010) edgeR: a Bioconductor package for differential expression analysis of digital gene expression data. *Bioinformatics* 26: 139-40
Sato Y, Kujirai T, Arai R, Asakawa H, Ohtsuki C, Horikoshi N, Yamagata K, Ueda J, Nagase T, Haraguchi T, Hiraoka Y, Kimura A, Kurumizaka H, Kimura H (2016) A Genetically Encoded Probe for Live-Cell Imaging of H4K20 Monomethylation. *J Mol Biol* 428: 3885-3902

Sato Y, Mukai M, Ueda J, Muraki M, Stasevich TJ, Horikoshi N, Kujirai T, Kita H, Kimura T, Hira S, Okada Y, Hayashi-Takanaka Y, Obuse C, Kurumizaka H, Kawahara A, Yamagata K, Nozaki N, Kimura H (2013) Genetically encoded system to track histone modification in vivo. *Sci Rep* 3: 2436
Schotta G, Sengupta R, Kubicek S, Malin S, Kauer M, Callen E, Celeste A, Pagani M, Opravil S, De La Rosa-Velazquez IA, Espejo A, Bedford MT, Nussenzweig A, Busslinger M, Jenuwein T (2008) A chromatin-wide transition to H4K20 monomethylation impairs genome integrity and programmed DNA rearrangements in the mouse. *Genes Dev* 22: 2048-61
Schulz EG, Meisig J, Nakamura T, Okamoto I, Sieber A, Picard C, Borensztein M, Saitou M, Bluthgen N, Heard E (2014) The Two Active X Chromosomes in Female ESCs Block Exit from the Pluripotent State by Modulating the ESC Signaling Network. *Cell Stem Cell* 14: 203-16
Shikata D, Yamamoto T, Honda S, Ikeda S, Minami N (2020) H4K20 monomethylation inhibition causes loss of genomic integrity in mouse preimplantation embryos. *J Reprod Dev*
Silva J, Mak W, Zvetkova I, Appanah R, Nesterova TB, Webster Z, Peters AH, Jenuwein T, Otte AP, Brockdorff N (2003) Establishment of histone h3 methylation on the inactive X chromosome requires transient recruitment of Eed-Enx1 polycomb group complexes. *Dev Cell* 4: 481-95
Stasevich TJ, Hayashi-Takanaka Y, Sato Y, Maehara K, Ohkawa Y, Sakata-Sogawa K, Tokunaga M, Nagase T, Nozaki N, McNally JG, Kimura H (2014) Regulation of RNA polymerase II activation by histone acetylation in single living cells. *Nature* 516: 272-5
Trojer P, Li G, Sims RJ, 3rd, Vaquero A, Kalakonda N, Boccuni P, Lee D, Erdjument-Bromage H, Tempst P, Nimer SD, Wang YH, Reinberg D (2007) L3MBTL1, a histone-methylation-dependent chromatin lock. *Cell* 129: 915-28
van Nuland R, Gozani O (2016) Histone H4 Lysine 20 (H4K20) Methylation, Expanding the Signaling Potential of the Proteome One Methyl Moiety at a Time. *Mol Cell Proteomics* 15: 755-64
Veloso A, Kirkconnell KS, Magnuson B, Biewen B, Paulsen MT, Wilson TE, Ljungman M (2014) Rate of elongation by RNA polymerase II is associated with specific gene features and epigenetic modifications. *Genome Res* 24: 896-905
Wilson DS, Keefe AD (2000) Random Mutagenesis by PCR. *Current Protocols in Molecular Biology* 51: 8.3.1-8.3.9
Wu S, Wang W, Kong X, Congdon LM, Yokomori K, Kirschner MW, Rice JC (2010) Dynamic regulation of the PR-Set7 histone methyltransferase is required for normal cell cycle progression. *Genes Dev* 24: 2531-42
Wutz A, Rasmussen TP, Jaenisch R (2002) Chromosomal silencing and localization are mediated by different domains of Xist RNA. *Nat Genet* 30: 167-74
Zylicz JJ, Bousard A, Zumer K, Dossin F, Mohammad E, da Rocha ST, Schwalb B, Syx L, Dingli F, Loew D, Cramer P, Heard E (2019) The Implication of Early Chromatin Changes in X Chromosome Inactivation. *Cell* 176: 182-197 e23
Zylicz JJ, Dietmann S, Gunesdogan U, Hackett JA, Cougot D, Lee C, Surani MA (2015) Chromatin dynamics and the role of G9a in gene regulation and enhancer silencing during early mouse development. *Elife* 4
Zylicz JJ, Heard E (2020) Molecular Mechanisms of Facultative Heterochromatin Formation: An X-Chromosome Perspective. *Annu Rev Biochem*

Figure legends

Figure 1. Establishing H3K27me3 mintbody to visualize H3K27me3 in living cells.
(**A**) Schematic representation of the mintbody. H3K27me3-specific single-chain variable fragment (scFv) is genetically fused with a fluorescent protein (FP).
(**B**) Immunofluorescence (IF) validation of mintbody specificity. Mouse MC12 cells, which stably express H3K27me3-mintbody (sfGFP), are labelled with antibodies specific for

H3K27me3 (Cy5) and H3K9me3 (Cy3). DNA is stained with Hoechst33342. Single confocal sections are shown.
(**C**) Time-lapse imaging of a dividing MC12 cell stably expressing H3K27me3-mintbody (sfGFP). Projection images of 7 confocal sections with 2µm intervals are shown with elapsed time (hh:mm).

Figure 2. Simultaneous visualisation of histone marks and X-chromosome loci in living cells.
(**A**) Schematic diagram of CRISPR/dCas9-3×sfGFP targeting loci on mouse X chromosome. sgRNA mX26 and mX8 target microsatellite repeats on *Dxz4* and *Xist* loci, respectively.
(**B**) Experimental design: female ESCs are engineered to stably express two sgRNAs, dCas9-3xsfGFP, and a nuclear localization signal (NLS)-fused H3K27me3-mintbody (mCherry). Upon ESC differentiation by LIF withdrawal H3K27me3 accumulation occurs at the inactivating X (Xi) but not at the active X (Xa). Green foci allow marking of two X-linked loci (*Dxz4* and *Xist*).
(**C**) Live imaging of female mESCs as in (B) in undifferentiated conditions (+LIF) or upon 3 days of LIF withdrawal. Double arrowheads mark Xa and single arrowhead marks Xi. Shown are maximum intensity projections of 11 z-plane confocal sections. Scale bar = 10 µm.
(**D**) ESCs as in (B) were engineered to also express H4K20me1-mintbody (Halo/JF646). Cells were cultured in the absence of LIF for 2 days. Time lapse images for 12 z-plane confocal stack were acquired every 1 h. Maximum intensity projection images are shown with elapse time (hh:mm). Arrowheads mark Xi. Scale bar = 10 µm

Figure 3. Simultaneous visualisation of histone marks and *Xist* RNA in living cells.
(**A**) Schematic representation of the experimental design. Female mouse ESC line was used, in which *Xist* can be induced from one allele (TX1072) and this allele also harbours an array of 18 Bgl stem loops (BglSL) inserted into the 7th exon of *Xist* gene. BglG fused to a fluorescent protein (GFP or mCherry) detects *Xist* RNA as it binds to BglSL. Cells also stably express a mintbody allowing the detection of H3K27me3 (GFP) or H4K20me1 (mCherry).
(**B**) Cells were treated with DOX to induce *Xist* expression for 1hrs and time laps imaging was performed with images acquired every 15 min. Maximum intensity projection images are shown with elapse time (hh:mm). Arrowheads mark Xi accumulating *Xist* RNA. Scale bar = 10 µm.
(**C**) Live-imaging analysis of average H3K27me3 (red) and H4K20me1 (blue) accumulation at the Xi. Average normalised mintbody enrichment is shown with shading representing 25 and 75 quartiles. Signal was calculated starting from the first accumulation of *Xist* RNA. At least 30 cells were analysed. Scale bar = 5 µm.

Figure 4. Native ChIP-seq reveals H4K20me1 and H3K27me3 co-accumulation during XCI.
(**A**) Schematic representation of the experimental design. The hybrid TX1072 mouse female ESC line was used, in which *Xist* can be induced from the endogenous B6 allele. Time course nChiP-seq for H4K20me1 was performed and compared to a published H3K27me3 dataset (GSE116480)(Zylicz et al., 2019).
(**B**) Quantification of average H4K20me1 (blue) and H3K27me3 (red) enrichment at the Xi (B6 allele) compared with t = 0 hr in 10-kb windows spanning the whole chromosome. Shading is the interquartile range.
(**C**) As in (B) but shown is normalised B6 enrichment to the average accumulation at 24 hrs.
(**D**) Pairwise comparison of H4K20me1 and H3K27me3 accumulation dynamics (ED50) at the X chromosome. All 10-kb windows with ED50 < 24 hr are plotted. The p-value is from a paired Wilcoxon rank sum test.
(**E**) H4K20me1 (blue) and H3K27me3 (red) accumulation across the Xi after 12 hr of DOX treatment. The black line is a locally estimated scatterplot smoothing (LOESS) regression on all 10-kb windows (dots). Bellow each plot shown is the *Xist* locus (green bar) and *Xist* entry sites (black bars).

(**F**) Correlation between H3K27me3 and H4K20me1 accumulation after 24hr of DOX treatment at initially active gene bodies (left), inactive gene bodies (middle) and 10-kb intergenic windows spanning the X chromosome (right). All scales are logarithmic. All correlations (ρ) are with p<0.01 from Pearson's correlation test.

Figure 5. H4K20me1 accumulates intergenically and relies on *Xist B+C* repeat region.
(**A**) Genome browser tracks showing H3K27me3 (top) and H4K20me1 (bottom) accumulation at a gene silenced rapidly (*Rnf12*) or more slowly (*Pgk1*). Allele-specific tracks were overlaid (B6 in red and Cast in blue). Note strong H4K20me1 bi-allelic pre-marking at gene bodies.
(**B**) Average H3K27me3 (top) and H4K20me1 (bottom) enrichment at the B6 allele over initially active or inactive genes ± 30kb at the X chromosome. Shown is data for all time points.
(**C**) Average H4K20me1 enrichment at the B6 allele over early and late silenced genes ± 30kb at the X chromosome. Shown is data for all time points. TSS : transcription start site ; TES : transcript end site.
(**D**) Schematic representation of the experimental design. By DOX addition, male TXY mouse ESC lines allow for expression of full length *XistFL* or *XistΔBC*. DOX-induced cells were used for combined IF and RNA FISH.
(**E**) Representative image of IF/RNA FISH for *Xist* RNA and H4K20me1 in cells expressing *XistFL* or *XistΔBC*. Arrowheads point to the *Xist* RNA domains.
(**F**) Graph represents the mean % +/- StDev of *Xist* RNA domains enriched for H4K20me1 (left) or H3K27me3 (right) in cells expressing *XistWT* or *XistΔBC*. Shown are averages from at least 2 independent experiments; minimum of 50 *Xist* RNA domains were counted per experiment; only P-values corresponding to significant differences from unpaired Student's t-test comparing mutants to *Xist* FL are indicated as * (P-value < 0.05). Data for H3K27me3 was extracted from published data (Bousard et al., 2019).

Expanded View Figure legends

Figure EV1. Establishing H3K27me3 mintbody to visualize H3K27me3 in living cells.
(**A**) Amino acid sequence of the scFv region of H3K27me3-mintbody derived from clone 2E12. Two amino acids that are substituted from the original 2E12 sequence are indicated with the regions of heavy and light chain variable fragments (VH and VL).
(**B**) Distribution of mintbody clones. Shown are single confocal sections of living mouse MC12 cells that transiently express mintbodies (sfGFP) from the original 2E12 and single (M86L) and double (M86L M158I) mutants. Scale bar = 10 µm.
(C) Model structures of 2E12 scFv. The 2E12 scFv structure was generated using ABodyBuilder(Leem, Dunbar et al., 2016) and the sites of substituted amino acid residues (colored in orange) are indicated with the zoomed view. Substitutions from Met86 to Leu and Met158 to Ile can fill the gap (red arrows) and stabilize the hydrophobic cores in heavy (M86L) and light (M158I) chains.

Figure EV2. Characterization of H3K27me3-mintbody.
(**A**) SDS-polyacrylamide gel analysis of purified mintbody. MBP-tagged H3K27me3-mintbody was expressed in and purified from E. coli through maltose-resin. After the removal of MBP moiety, H3K27me3-mintbody was separated on a 10-20% SDS-polyacrylamide gel and stained with Commassie Brilliant Blue.
(**B**) Peptide array analysis. A MODified Histone Array (Active Motif) was probed with the purified H3K27me3-mintbody followed by peroxidase-conjugated anti-GFP antibody. Peptides containing H3K27me3, except one with H3S28ph, were highlighted.
(**C-F**) Immunofluorescence. HeLa cells were transfected with expression vectors to transiently express Halotag-tagged KDM6B (C and E) and KDM4D (D and F), fixed, and stained with antibodies specific for H3K27me3 (C) and H3K9me3 (D), or H3K27me3-

mintbody (E and F). Fluorescence intensities in individual nuclei were measured and dot plotted. Transfected cells are indicated by arrowheads. Cells expressing KDM6B and KDM4D showed decreased levels of H3K27me3 (C) and H3K9me3 (D), respectively, by antibody staining. H3K27me3-mintbody signals were lower in cells expressing KDM6B (E) but not KDM4D (F).

Figure EV3. Labelling X-linked loci by sgRNA-dCas9 system
(**A**) Schematic diagram of CRISPR/dCas9-3×sfGFP targeting loci on the mouse X chromosome.
(**B, C**) IF validation of sgRNAs targeting X-linked loci. Mouse MC12 cells that stably express sgRNA and dCas9-EGFP were fixed and stained with antibody specific for H3K27me3 (Cy5) and Hoechst33342. Shown are cells in interphase (B; maximum intensity projections of 7 z-plane confocal sections) and in mitosis (C; 30 z-sections). Arrowheads and arrow indicate Xa and Xi, respectively. In MC12 cells, the inactive X chromosome is known to have a translocation to an autosome at the distal end and probably lacks mX2 target sequence. Scale bar = 10 µm.

Figure EV4. System to simultaneously visualise H3K27me3 or H4K20me1 and *Xist* RNA in living cells.
(**A**) Schematic representation of the TX-BglSL parental line obtained previously (Dossin et al., 2020). This system is based on the TX1072 female hybrid ESC line where *Xist* is induced by DOX treatment from the endogenous B6 allele. In TX-BglSL 18 Bgl stem loops have been knocked-in into the 7th exon of *Xist*.
(**B**) Schematic representation of the TX-Bgl-EGFP; H4K20me1-mCherry ESC line. This line is derived from TX-BglSL by knocking-in BglG-EGFP expression cassette into Rosa 26 locus. Homologous recombination was aided by using nickase Cas9 protein and two gRNAs targeting Rosa 26. Knock-in can occur only at one allele as the other one contains the rTTA element allowing for DOX inducible expression of *Xist* RNA. Stable lines expressing H4K20me1 specific mintbody fused to mCherry were generating by random insertion of a PiggyBac vector (bottom).
(**C**) Schematic representation of the TX-Bgl-mCherry; H3K27me3-sfGFP ESC line. This line is derived from TX-BglSL by knocking-in BglG-mCherry expression cassette into Tigre locus. Homologous recombination was aided by using wildtype Cas9 protein and a single gRNA targeting Tigre. Stable lines expressing H3K27me3 specific mintbody fused to sfGFP were generated by random insertion of a PiggyBac vector (bottom).
(**D**) Validation of efficient X chromosome inactivation in TX-Bgl-EGFP; H4K20me1-mCherry and TX-Bgl-mCherry; H3K27me3-sfGFP ESC lines. Cells were treated with DOX for 0 or 24hrs; pyrosequencing was performed from cDNAs. Allelic ratios of two X-linked genes (*Rnf12* and *AtrX*) was measured. Note comparable levels of gene silencing in both clones.

Figure EV5. H4K20me1 native ChIP-seq controls.
(**A**) Peptide array analysis of anti-H4K20me1 antibody (5E10-D8) used for native ChIP-seq. A MODified Histone Array (Active Motif) was probed with the anti-H4K20me1 antibody (5E10-D8). All peptides containing H4K20me1 were highlighted.
(B) Bar plot showing the percentage of B6 reads mapping to the X chromosome in the nChIP-seq time course.
(C) Relating to Fig. 5B. Average H3K27me3 (top) and H4K20me1 (bottom) enrichment at the B6 allele over active or inactive genes ± 30kb on autosomes. Shown is data for all time points. Note enrichment of H4K20me1 at active genes and the stability of the signal between all time points.

Supplementary table 1. Target sequence candidates for labeling X-linked loci
X chromosome specific spots were detected for 7 gRNAs in cells expressing them transiently. Four cells lines (for mX2, mX8, mX18, and mX26) were able to be established. ND, not detectable.

Movie EV1. Live-imaging of H3K27me3-mintbody in MC12 cell
MC12 cells expressing H3K27me3-mintbody were imaged every 15 min. Maximum intensity projections of 7 z-planes with 2 µm intervals are shown. Elapsed time is indicated as hh:mm.

Movie EV2. Live-imaging of H3K27me3-mintbody in TX-*Xist*-mCherry ESCs during XCI
TX-*Xist*-mCherry ESCs expressing H3K27me3-sfGFP mintbody were treated with DOX to induce *Xist* expression. About 1hr after DOX addition cells were imaged every 15 min for 6 hrs. Maximum intensity projections are shown. *Xist* RNA, detected by BglG, is in green and mintbody channel in red. Elapsed time is indicated as fractions of hrs. Bar code = 10um.

Movie EV3. Live-imaging of H4K20me1-mintbody in TX-*Xist*-EGFP ESCs during XCI
TX-*Xist*-EGFP ESCs expressing H4K20me1-mCherry mintbody were treated with DOX to induce *Xist* expression. About 1hr after DOX addition cells were imaged every 15 min for 6 hrs. Maximum intensity projections are shown. *Xist* RNA, detected by BglG, is in green and mintbody channel in red. Elapsed time is indicated as fractions of hrs. Bar code = 10um.

Fig. 1

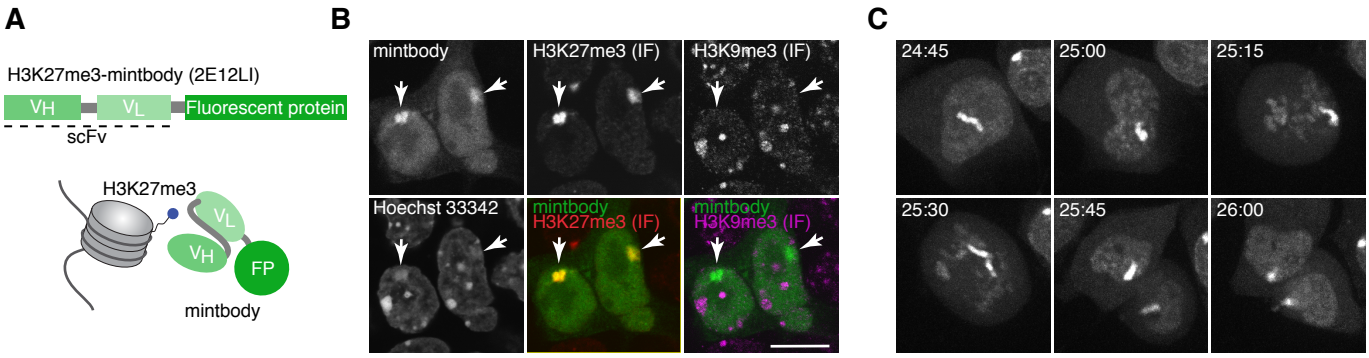

Figure 1. Establishing H3K27me3 mintbody to visualize H3K27me3 in living cells.
(A) Schematic representation of the mintbody. H3K27me3-specific single-chain variable fragment (scFv) is genetically fused with a fluorescent protein (FP).
(B) Immunofluorescence (IF) validation of mintbody specificity. Mouse MC12 cells, which stably express H3K27me3-mintbody (sfGFP), are labelled with antibodies specific for H3K27me3 (Cy5) and H3K9me3 (Cy3). DNA is stained with Hoechst33342. Single confocal sections are shown.
(C) Time-lapse imaging of a dividing MC12 cell stably expressing H3K27me3-mintbody (sfGFP). Projection images of 7 confocal sections with 2µm intervals are shown with elapsed time (hh:mm).

Fig. 2

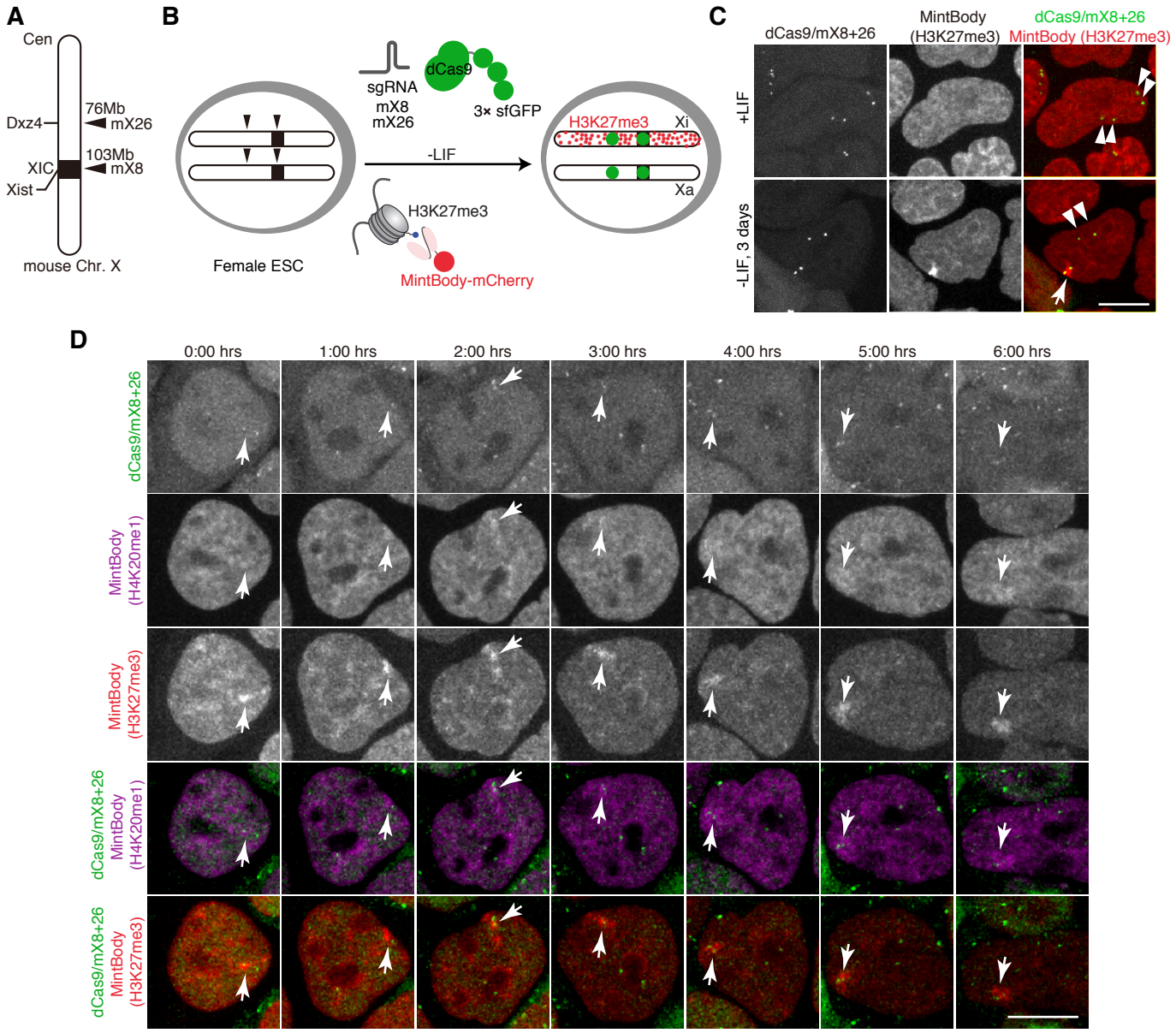

Figure 2. Simultaneous visualisation of histone marks and X-chromosome loci in living cells.
(A) Schematic diagram of CRISPR/dCas9-3×sfGFP targeting loci on mouse X chromosome. sgRNA mX26 and mX8 target microsatellite repeats on Dxz4 and Xist loci, respectively.
(B) Experimental design: female ESCs are engineered to stably express two sgRNAs, dCas9-3xsfGFP, and a nuclear localization signal (NLS)-fused H3K27me3-mintbody (mCherry). Upon ESC differentiation by LIF withdrawal H3K27me3 accumulation occurs at the inactivating X (Xi) but not at the active X (Xa). Green foci allow marking of two X-linked loci (Dxz4 and Xist).
(C) Live imaging of female mESCs as in (B) in undifferentiated conditions (+LIF) or upon 3 days of LIF withdrawal. Double arrowheads mark Xa and single arrowhead marks Xi. Shown are maximum intensity projections of 11 z-plane confocal sections. Scale bar = 10 µm.
(D) ESCs as in (B) were engineered to also express H4K20me1-mintbody (Halo/JF646). Cells were cultured in the absence of LIF for 2 days. Time lapse images for 12 z-plane confocal stack were acquired every 1 h. Maximum intensity projection images are shown with elapse time (hh:mm). Arrowheads mark Xi. Scale bar = 10 µm

Fig. 3

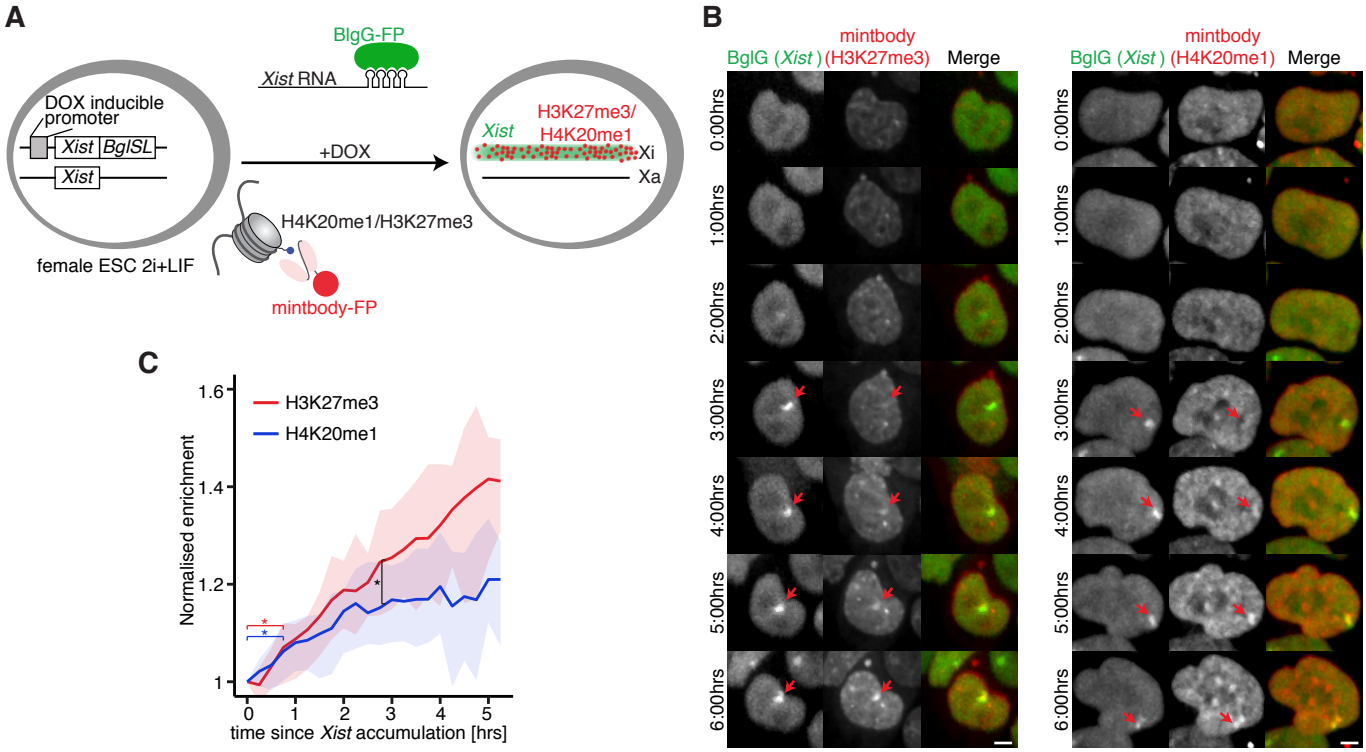

Figure 3. Simultaneous visualisation of histone marks and Xist RNA in living cells.
(A) Schematic representation of the experimental design. Female mouse ESC line was used, in which Xist can be induced from one allele (TX1072) and this allele also harbours an array of 18 Bgl stem loops (BglSL) inserted into the 7th exon of Xist gene. BglG fused to a fluorescent protein (GFP or mCherry) detects Xist RNA as it binds to BglSL. Cells also stably express a mintbody allowing the detection of H3K27me3 (GFP) or H4K20me1 (mCherry).
(B) Cells were treated with DOX to induce Xist expression for 1hrs and time laps imaging was performed with images acquired every 15 min. Maximum intensity projection images are shown with elapse time (hh:mm). Arrowheads mark Xi accumulating Xist RNA. Scale bar = 10 µm.
(C) Live-imaging analysis of average H3K27me3 (red) and H4K20me1 (blue) accumulation at the Xi. Average normalised mintbody enrichment is shown with shading representing 25 and 75 quartiles. Signal was calculated starting from the first accumulation of Xist RNA. At least 30 cells were analysed. Scale bar = 5 µm.

Fig. 4

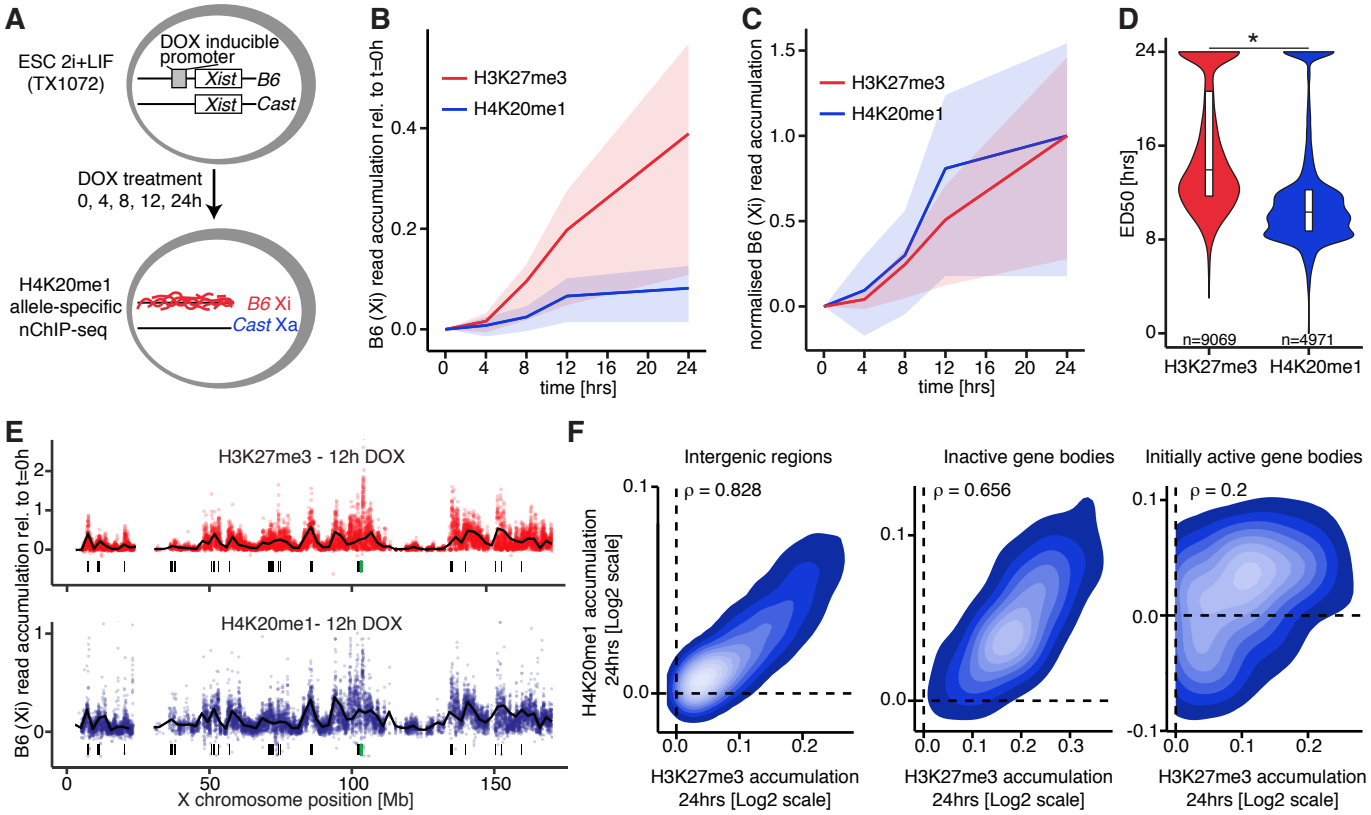

Figure 4. Native ChIP-seq reveals H4K20me1 and H3K27me3 co-accumulation during XCI.
(A) Schematic representation of the experimental design. The hybrid TX1072 mouse female ESC line was used, in which Xist can be induced from the endogenous B6 allele. Time course nChiP-seq for H4K20me1 was performed and compared to a published H3K27me3 dataset (GSE116480)(Zylicz et al., 2019).
(B) Quantification of average H4K20me1 (blue) and H3K27me3 (red) enrichment at the Xi (B6 allele) compared with t = 0 hr in 10-kb windows spanning the whole chromosome. Shading is the interquartile range.
(C) As in (B) but shown is normalised B6 enrichment to the average accumulation at 24 hrs. (D) Pairwise comparison of H4K20me1 and H3K27me3 accumulation dynamics (ED50) at the X chromosome. All 10-kb windows with ED50 < 24 hr are plotted. The p-value is from a paired Wilcoxon rank sum test.
(E) H4K20me1 (blue) and H3K27me3 (red) accumulation across the Xi after 12 hr of DOX treatment. The black line is a locally estimated scatterplot smoothing (LOESS) regression on all 10-kb windows (dots). Bellow each plot shown is the Xist locus (green bar) and Xist entry sites (black bars).
(F) Correlation between H3K27me3 and H4K20me1 accumulation after 24hr of DOX treatment at initially active gene bodies (left), inactive gene bodies (middle) and 10-kb intergenic windows spanning the X chromosome (right). All scales are logarithmic. All correlations (ρ) are with p<0.01 from Pearson's correlation test.

Fig. 5

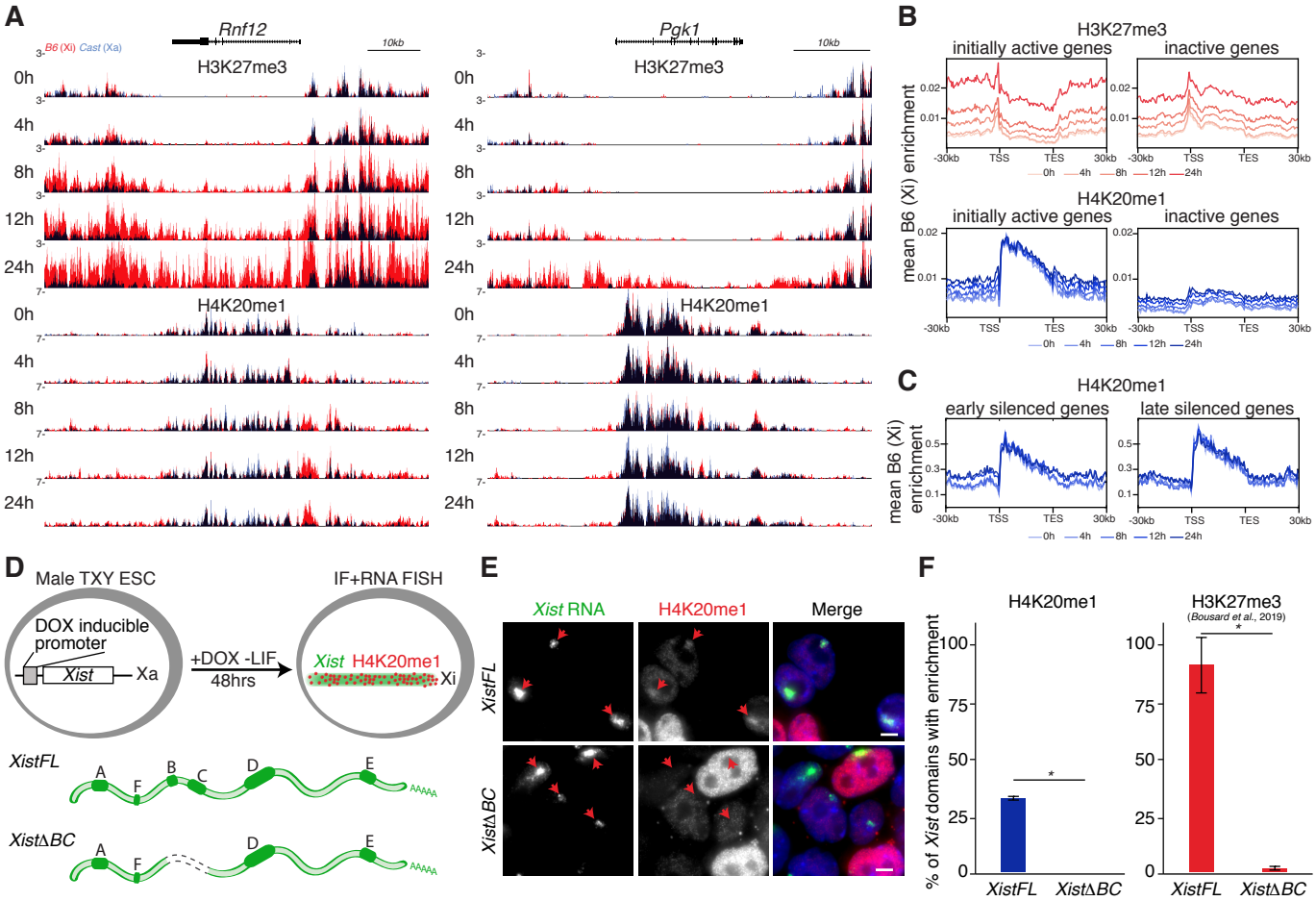

Figure 5. H4K20me1 accumulates intergenically and relies on Xist B+C repeat region.
(A) Genome browser tracks showing H3K27me3 (top) and H4K20me1 (bottom) accumulation at a gene silenced rapidly (Rnf12) or more slowly (Pgk1). Allele-specific tracks were overlaid (B6 in red and Cast in blue). Note strong H4K20me1 bi-allelic pre-marking at gene bodies.
(B) Average H3K27me3 (top) and H4K20me1 (bottom) enrichment at the B6 allele over initially active or inactive genes ± 30kb at the X chromosome. Shown is data for all time points.
(C) Average H4K20me1 enrichment at the B6 allele over early and late silenced genes ± 30kb at the X chromosome. Shown is data for all time points. TSS : transcription start site ; TES : transcript end site.
(D) Schematic representation of the experimental design. By DOX addition, male TXY mouse ESC lines allow for expression of full length XistFL or XistΔBC. DOX-induced cells were used for combined IF and RNA FISH.
(E) Representative image of IF/RNA FISH for Xist RNA and H4K20me1 in cells expressing XistFL or Xist ΔBC. Arrowheads point to the Xist RNA domains.
(F) Graph represents the mean % +/- StDev of Xist RNA domains enriched for H4K20me1 (left) or H3K27me3 (right) in cells expressing XistWT or XistΔBC. Shown are averages from at least 2 independent experiments; minimum of 50 Xist RNA domains were counted per experiment; only P-values corresponding to significant differences from unpaired Student's t-test comparing mutants to Xist FL are indicated as * (P-value < 0.05). Data for H3K27me3 was extracted from published data (Bousard et al., 2019).